iScience

CellPress
OPEN ACCESS

Review

Resonant inelastic X-ray scattering for studying materials for renewable energy conversion and storage

Rongfu Hong,[1,6] Lixin Xing,[1,6] Mingjie Wu,[2] Zhangsen Chen,[3] Ning Wang,[1] Ling Meng,[1] Siyu Ye,[1] Liguang Wang,[4] Gaixia Zhang,[5,*] and Lei Du[1,*]

[1]Huangpu Hydrogen Energy Innovation Centre/School of Chemistry and Chemical Engineering, Guangzhou University, Guangzhou 510006, P.R. China
[2]State Key Laboratory of New Textile Materials and Advanced Processing Technologies, Wuhan Textile University, Wuhan 430200, P.R. China
[3]Institut National de la Recherche Scientifique-Énergie Matériaux et Télécommunications, Varennes, QC J3X 1S2, Canada
[4]College of Chemical and Biological Engineering, Zhejiang University, Hangzhou 310058, P.R. China
[5]Department of Electrical Engineering, École de Technologie Supérieure (ÉTS), Montréal, QC H3C 1K3, Canada
[6]These authors contributed equally
*Correspondence: gaixia.zhang@etsmtl.ca (G.Z.), lei.du@gzhu.edu.cn (L.D.)

https://doi.org/10.1016/j.isci.2025.112820

SUMMARY

Renewable energy conversion and storage technologies, including batteries, fuel cells, and electrolyzers, have garnered global attention. Electrode materials are crucial in determining the performance and lifespan of the corresponding devices. Transition metals and light elements are key components in electrode materials, enabling efficient energy conversion by directly providing active sites or indirectly optimizing material electronic structures. To understand the relationship between electronic structures and device performance, advanced techniques like X-ray absorption spectroscopy (XAS) have been developed. Recently, resonant inelastic X-ray scattering (RIXS) features coupled with X-ray emission spectra (XES) have emerged as a complementary tool, providing additional insights into material electronic structures. This review focuses on recent advances in using XES, particularly RIXS, for studying energy conversion and storage materials, highlighting the unique features and potential of RIXS for electronic structure characterization and quantitative analysis. This work aims to stimulate interests in utilizing RIXS features in the field of energy conversion and storage.

INTRODUCTION

Renewable energy conversion and storage applications are essential in our daily lives: one can convert chemical energy into electric energy; while the other is responsible for storing electric energy, produced from renewable resources like solar energy and wind energy, by converting electric energy into chemical bonds. Well-designed energy conversion and storage applications, including batteries, fuel cells, and electrolyzers, universally require high-performance and stable electrode/catalyst materials.[1–8]

Great efforts have been made to develop innovative materials for energy conversion and storage applications.[9–11] Generally, the transition metals (TM) play important roles in the key materials for these applications (e.g., Mn, Co, and Ni for the Li-ion batteries,[7,11–15] Pt, Fe, Mn, and Co for the fuel cells;[16–20] Ir, Mn, Fe, Ni, and Co for the electrolyzers[21–24]). The TM elements that are located in Groups IIIB to VI, IB, and IIB in the periodic table share a universal electronic structure of [inert gas](n-1)$d^{1\text{-}10}ns^{0\text{-}2}$, which can also be named d-block elements such as Mn: [Ar] $3d^5 4s^2$. The electronic structure of TMs is a significant factor in determining the performance of energy conversion and storage devices.[13,25–29] On the other hand, the electronic structure of light elements, such as C, N, and O, also matters for energy conversion and storage, e.g., oxygen redox for batteries,[30–34] nitrogen dopant moieties[35–39] and oxygen vacancies[40,41] for photo-, electro-catalysis. To rationally design ideal electrode/catalyst materials, the relationship between the electronic structure of key elements and the properties of corresponding materials needs to be revealed; it is also necessary to study the tiny electronic-structure changes of the key elements during device operation to understand the degradation mechanisms.

A lot of advanced techniques have been developed and applied to investigate the electronic structure of materials, such as X-ray photoelectron spectroscopy (XPS),[15,42,43] ultraviolet photoelectron spectroscopy (UPS),[44,45] and X-ray absorption spectroscopy (XAS).[22,46,47] In recent studies, resonant inelastic X-ray scattering (RIXS) has been emerging as a powerful tool to investigate the electronic structure for both TM and light elements that are difficult to study by conventional methods such as XPS and UPS. We note that RIXS is effectively a resonant form of X-ray emission spectroscopy (XES).[48–56] Due to the rapid development of the high-flux synchrotron light sources, compared to traditional X-ray absorption near edge structures (XANES) and extended X-ray absorption fine structures (EXAFS), the RIXS characteristics of XES can occasionally provide additional information. This information is closely related to subtle changes in electronic structure, such as feature energies that are not apparent in the pre-edge of soft X-ray absorption spectroscopy (sXAS) but do appear in the soft X-ray mapping of resonant inelastic X-ray scattering (mRIXS).[29,57]

Over decades of advancement, RIXS has been progressively gaining recognition as a powerful spectroscopic technique in the energy conversion and storage field.[6–8,10,49,58–62] Here, we focus on the advancements in the application of RIXS features in this field. In this review, RIXS will be briefly introduced and some of its unique features will be described. Then, the inspiring achievements of applying RIXS features in studying electronic structures, monitoring their changes during operation, and quantitative analysis will be discussed. With the basic knowledge of RIXS provided by this review, we hope to spark the interest of the community to further explore the application of RIXS in their studies.

BRIEF INTRODUCTION TO RIXS

As mentioned above, advanced techniques including XPS, UPS, and XAS have been developed and widely applied in studying the electronic structures of materials for renewable energy conversion and storage. In principle, to investigate the electronic structure, the photon with specific energy (e.g., X-ray for XPS and XAS, ultraviolet light for UPS) is needed to excite the core electron, which will jump to an excited state and leave a hole. When high-energy fixed-incident X-ray photons possess sufficient energy to eject excited electrons from the sample as photoelectrons, XPS spectra are obtained. Conversely, by utilizing tunable incident X-ray photons to excite electrons into unoccupied states, distinct absorption maxima emerge within specific photon energy ranges—this phenomenon defines the X-ray absorption near edge structure (XANES, a part of XAS).

XAS can be categorized into different types based on the testing energy range (soft X-ray, low-to medium-energy hard X-ray, and high-energy hard X-ray). The widely used K edge hard XAS (hXAS) can detect the redox state of TM by analyzing the energy shift of the absorption edge. However, this information is not directly related to the 3d valence state of TM (1s state to 4p state). Information about the TM 3d orbital might be hidden in the pre-edge and white-line region. On the other hand, the soft XAS (sXAS) can monitor the L edge of TM, which directly reflects the excitations to 3d states (2p state to 3d state). Although sXAS offers higher sensitivity compared to hXAS, it has a relatively small probe depth. Besides, sXAS usually requires high vacuum conditions, which makes *in situ* and operando experiments complicated. Even though the fluorescence yield (FY) mode of sXAS can reach a large detection depth of several hundred nanometers,[57,58,63] the distortion of the lineshape of the photon-in-photon-out (PIPO) channel with bulk signals leads to unreliable results in analyzing the properties of emitted photons and the reflected electronic structures. A major reason for distortion is the self-absorption of fluorescence by the sample itself,[63] which affects the intensity of the fluorescence signal. This self-absorption effect is particularly evident in thicker samples, resulting in a non-linear energy relationship between the signal and the absorption edge. Although thinning samples can be employed to improve matters, existing research emphasizes the importance of *in situ*/operando experiments, suggesting that thinning samples may not be adequate for all situations.

Typically, XAS measurements collect information regarding the number of emitted electrons and photons but fail to get information on the energy distribution of emitted photons. In addition, the XAS spanning from 50 to 1500 eV has limitations in studying the electronic structures of light elements such as C, N, and O because it generally provides XANES data but without access to the EXAFS data, which is crucial for studying the atomic coordination environment. Light elements have smaller atomic numbers, resulting in relatively low binding energies for their inner-shell electrons. When X-ray photons interact with these elements, the photon energy is readily absorbed, causing the excitation or ionization of inner-shell electrons. Nonetheless, due to the lighter atomic mass of light elements, their scattering cross-sections are relatively small, leading to weaker scattering signal intensities. As a result, signals of light elements in XAS experiments are prone to being obscured by background noise, thereby increasing the difficulty in data analysis and interpretation.

Fortunately, the XES technique allows for the collection of RIXS signals, which can monitor the energy distribution of emitted photons at each incident photon energy. When the energy of the scattered photon depends on that of the incident photon, and there is a mismatch between them (indicating energy loss or transfer), RIXS occurs.[64,65] In this case, RIXS can be considered as a combination of X-ray absorption and emission spectroscopies, and the mRIXS data also provides emission energy information that is completely missing from traditional XAS spectra. Therefore, the TM L edge mRIXS data is a two-dimensional map containing excitation energy, emission energy, and emission peak intensity information. The chemical state of TMs can be quantitatively evaluated through inverse partial FY analysis (mRIXS-iPFY), as the extracted mRIXS-iPFY spectrum displays a TM lineshape which is almost identical to that from surface sensitive electron yield signals, without any lineshape distortion. For instance, Mn L sXAS spectra in iPFY mode can be obtained by inverse integration of O K XES characteristics within the emission energies of 520–530 eV.[29] Furthermore, despite the ongoing challenges associated with X-ray-based characterization techniques in the analysis of light elements, recent advancements in utilizing mRIXS to characterize oxygen redox reaction processes in battery materials have been particularly noteworthy. By leveraging the high sensitivity and energy resolution of the RIXS technique, there is promising potential to further elucidate the fundamental mechanisms underlying these reactions as well as subtle variations in the chemical environment.

Essentially, the RIXS signal depends on a PIPO process, and it can be divided into direct and indirect RIXS processes according to the different scattering mechanisms (Figure 1).[66,67] In the direct process, X-rays are incident on the sample, electrons in deep-core levels, such as those in the K-shell or L-shell, absorb the energy of the incident photons thereby transitioning to

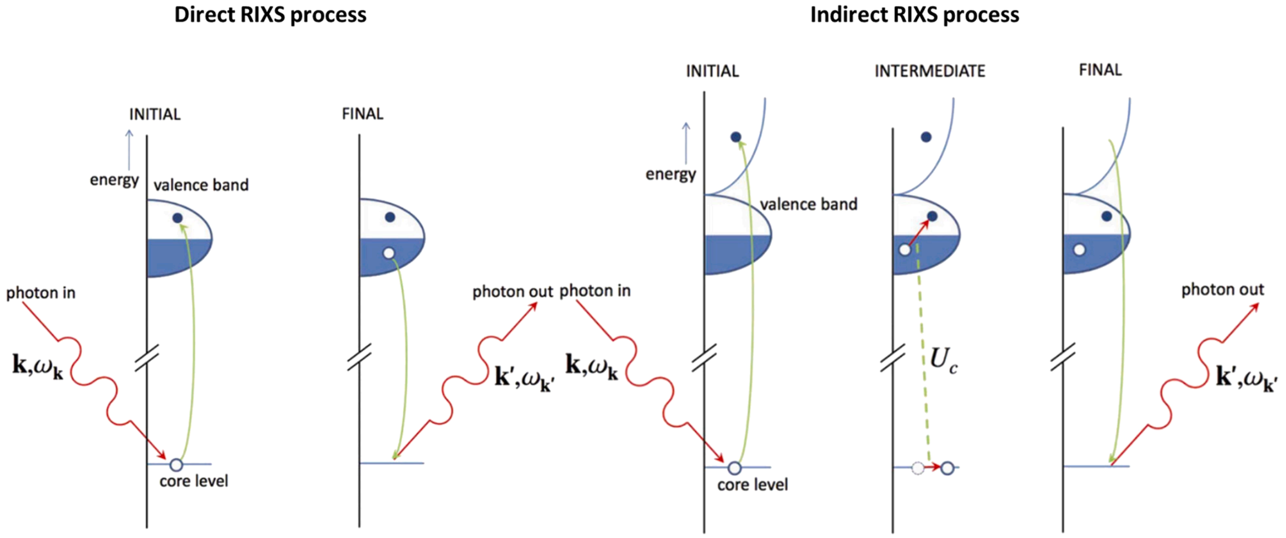

Figure 1. Illustration of the RIXS process

k and k′ represent the momentum of photons, ω_k and $\omega_{\mathrm{k}'}$ represent the energy of photons, U_c represents Coulomb interaction. Reproduced from ref.[66]

unoccupied orbitals in the valence band. This process is resonant, as the energy of the incident photon matches the specific transition energy of the electrons. The excitation of deep-core electrons creates vacancies in the originally filled orbitals, rendering the system unstable and often leading to a redistribution of electrons. To fill these vacancies, electrons from the valence band may transition to empty orbitals in the deep-core levels, releasing energy in the process. Consequently, inelastic scattering occurs, characterized by changes in the energy and momentum of the photons. Such information is invaluable for probing the electronic structure and excited states of the sample.

In the indirect RIXS process, incident photons excite core electrons (such as 1s electrons) to empty states above the Fermi level (such as 4p electrons). The excitation of core electrons leaves a core hole, which exerts a strong electric potential on the surrounding valence electrons (e.g., 3d electrons). This change in electric potential significantly influences the behavior of the valence electrons, making them more susceptible to scattering. In this process, transitions from the core state to conduction band states must be weak, otherwise a significant portion of the incident light energy will be utilized to directly excite core electrons to the conduction band state, rather than generating scattering signals through valence electrons.

Under the influence of core holes, valence electrons may become excited, resulting in the formation of electron-hole pairs. This excitation is a critical aspect of the indirect RIXS process, as it facilitates inelastic scattering. When electrons decay from the 4p state back to the 1s state, the core holes are filled, leading to the release of energy. This process is accompanied by the retention of electron-hole pairs, giving rise to exciton states. As the absorption edge is approached, the interaction between 1s core holes and 4p electrons can lead to the formation of excitons. However, the formation of excitons does not fundamentally alter the overall framework of indirect RIXS. The presence of excitons may introduce new scattering mechanisms, complicating the interactions between valence electrons and excitons.

The distinction between direct and indirect processes is crucial for understanding the electronic structure and excited states of materials. Direct RIXS typically provides clearer information about specific excited states, whereas indirect RIXS can reveal more complex multi-body interactions and dynamic processes. However, when direct scattering is allowed, it is the dominant inelastic scattering channel, with indirect processes contributing only through higher-order perturbation terms in multi-body interactions rather than direct electronic transitions.

THE UNIQUE FEATURES OF RIXS

As a promising supplement, RIXS, to some extent, can serve as an auxiliary of XAS and XES. The contributions of each emitted photon to the overall emission spectrum can be distinguished and recorded.[68] Figure 2A demonstrates the Co $L_{2,3}$ XAS edge (top panel) and the five Co 2p3d RXES (resonant X-ray emission spectroscopy, bottom panel) taken at the fixed excitation energies marked in the XAS in the top panel.[69] The peaks with the fixed energy loss values are typical features in RIXS that can be interpreted as d-d excitations, charge transfer, and charge fluctuation excitations. On the other hand, the peaks with varying energy loss values (fixed emission energy, marked with the dotted line in Figure 2A) are XRF (X-ray fluorescence) features that originate from the deexcitation of the intermediate state to a final state. Therefore, RIXS can reveal the energy distribution of the emitted photons at each incident energy. As shown in Figure 2B, the typical mRIXS (XES or RXES mapping) for CO_2 at the O K edge can provide many features (different colors represent different intensities). The intensity map in Figure 2B allows a quick observation of XRF (with fixed emission energies despite the excitation energies, i.e., B, C, D, E, G, and F spots in Figure 2B) and d-d excitation RIXS (with fixed energy

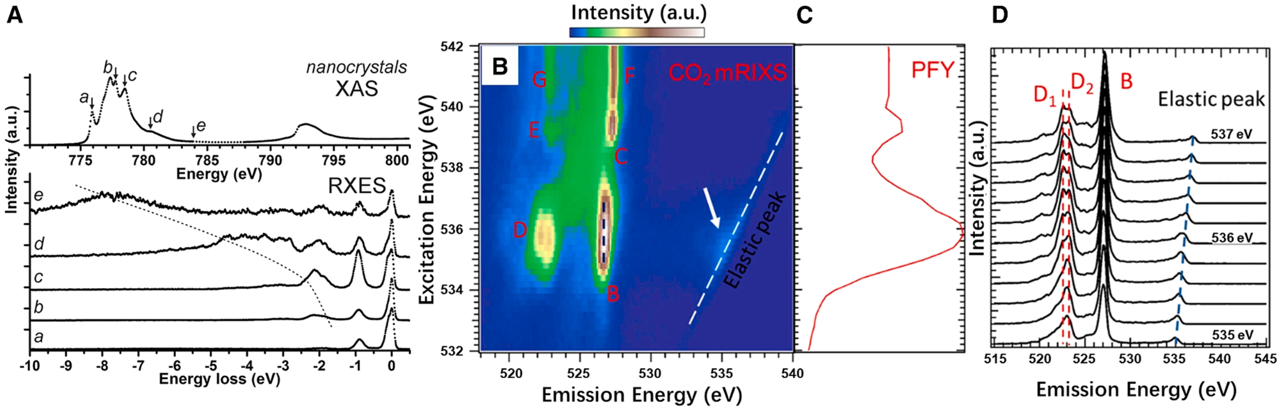

Figure 2. CoO nanocrystals and CO$_2$ spectral characterization via XAS and RXES (RIXS)

(A) Co $L_{2,3}$ XAS (top panel) and 2p3d RXES (bottom panel) for CoO nanocrystals at 291 K. The RXES spectra were acquired at five fixed excitation energies labeled a–e.

(B) O K edge mRIXS of CO$_2$. Seven groups of features are observed, as indicated by the white arrow on the low-energy excitations and the letters of B-G (Red font). Group D consists of two features D$_1$ and D$_2$.

(C) O K edge XAS-PFY (partial fluorescence yield mode) of CO$_2$, which is obtained by the integration of the RIXS signals at each excitation energy.

(D) Individual O K edge RIXS cuts of CO$_2$ with an excitation energy range of 535–537 eV of 0.2 eV step.

(A) Reproduced with permission.[69] Copyright 2012, American Chemical Society. (B–D) Reproduced with permission.[53] Copyright 2020, American Chemical Society.

loss, forming parallel peaks alongside the elastic peak, indicated by the white arrow in Figure 2B) peaks. The intensity of this XAS spectrum at a specific excitation energy (Figure 2C) is a sum of photons at different emission energies. By measuring the XES with different excitation energies, detailed peak information can be obtained, as depicted in Figure 2D, for further comprehensive analysis. The RIXS is thus sensitive to both elemental composition and chemical/electronic states to provide more information in terms of the bulk materials, interfaces, as well as light elements (C, N, O).

Here, we would like to highlight another example to support that the RIXS can provide what XAS cannot see. As shown in Figure 3A, there is almost no obvious difference in the XAS curves for water and KCl-water solutions in different concentrations (1 M, 2 M, and 3 M).[70] Interestingly, the corresponding mRIXS in Figure 3B show significant differences in the regions marked as C as the KCl concentration increases. Although we are not focused on the detailed analysis of the mRIXS in this work, as it is not directly related to energy conversion and storage, the maps still provide a compelling example that RIXS can provide important supplementary information compared to conventional techniques such as XAS to investigate tiny differences in the targeted system.

It should be noted that we do not belittle the conventional XAS technique, which is powerful and applicable in the study of materials. XAS can be collected in several seconds to upwards of a minute. However, the collection of RIXS information (a series of XES spectra) typically requires several hours or more, depending on the experimental setup and sample properties. Moreover, RIXS is inherently a technique with low signal-to-noise ratio and count rates, necessitating exceptionally high photon flux.[29,57,71] This naturally poses technical challenges, including achieving sufficient statistical significance within reasonable measurement times and mitigating radiation damage to the sample. Therefore, RIXS is not suitable for all scenarios. We emphasize that RIXS can be an excellent supplement when applicable. In the following sections, we will discuss the advances of using RIXS in studying key materials for energy conversion and storage, in terms of detecting electronic structures, investigating their changes during reactions, and quantifying spectral features to uncover the reaction mechanisms.

RIXS IN ANALYZING THE ELECTRONIC STRUCTURE OF ELECTRODE MATERIALS

The electronic structure usually plays a central role in determining the reaction kinetics and is thus pivotal for the rational design of materials for energy conversion and storage.[13,28,60,72–75] As mentioned above, more information can be obtained that cannot be obtained solely through XAS, with the help of RIXS. One of the most powerful capabilities of RIXS is its comprehensive information on electronic structures. In the field of energy conversion and storage, many reactions rely on precious metal catalysts such as Pt and Ir. How to improve the utilization, activity, and stability of these precious metals, while achieving cost reduction and efficiency enhancement, is one of the key challenges. Therefore, it is necessary to fully reveal the electronic structure information of the materials themselves and facilitate the understanding of the structure-activity relationship. The ongoing advancements in RIXS technique offer powerful tools for addressing these challenges.[28,60,75,76]

Below, we present an illustrative example demonstrating the electronic structure of Pt with and without CO adsorption. As shown in Figure 4A, the signal of valence band excitation for Pt merges with the elastic line where the energy loss is equal to 0 eV. Interestingly, upon on-site adsorption of a CO molecule (Figure 4B), the intensity peak shifts by ∼ 4 eV in energy loss.[60] This indicates an energy difference between the lowest

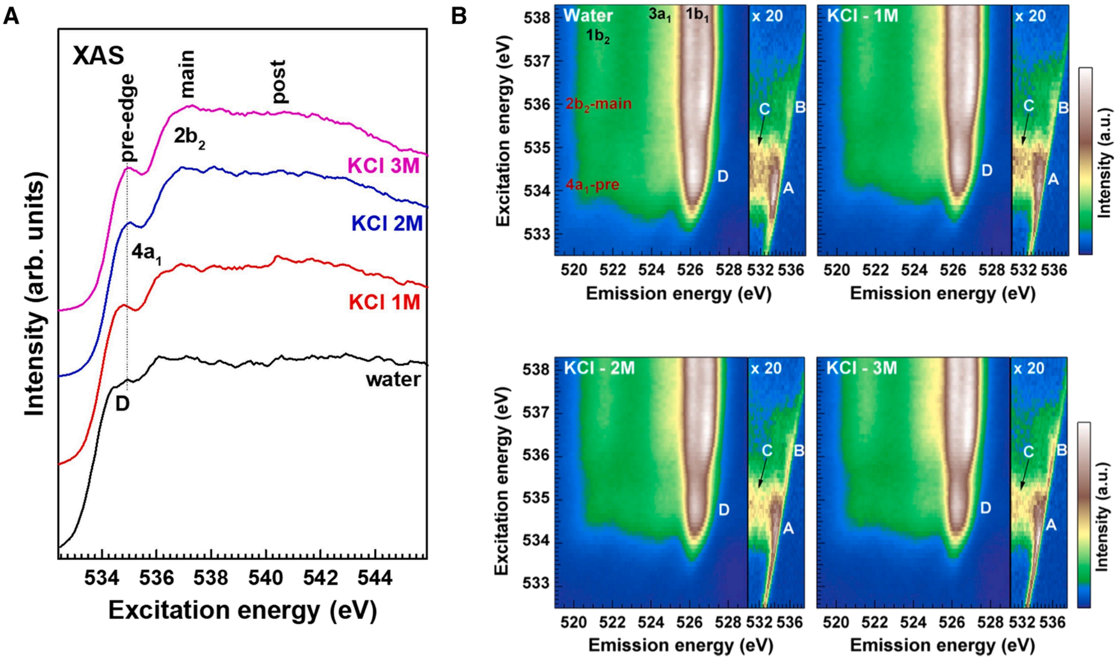

Figure 3. O K edge XAS and mRIXS of pure water and KCl-water solutions with different concentrations

(A) O K edge XAS at the pure water and the KCl-water solutions with different concentrations (1, 2 and 3 M) which are extracted from the mRIXS of Figure 3B. The XAS spectra represent the integrated intensity over an emission energy range of 519–529 eV. The label D corresponds to the same feature as in the mRIXS of Figure 3B.

(B) O K edge mRIXS at the pure water and the KCl-water solutions with different concentrations (1, 2 and 3 M). The emission intensity is demonstrated as a function of excitation and emission energies.

(A and B) Reproduced with permission.[70] Copyright 2014, American Chemical Society.

unoccupied state and the elastic line for Pt, suggesting that the adsorbed CO induces changes in electronic structure. Besides, by combining the theoretical mRIXS of different Pt-CO models and experimental results, the RIXS can also be utilized to determine the CO adsorption configurations on Pt surfaces. As shown in Figures 4C-4F, the mRIXS of a theoretical Pt_6 cluster and related Pt_6-CO in three different configurations are calculated. Compared with the pure Pt_6 cluster (Figure 4C), Pt_6-CO models with the bridged (Figure 4E) and face bridging (Figure 4F) configurations exhibit an upward shift; particularly, the CO adsorption in the atop configuration onto a single Pt atom (Figure 4D) leads to the most significant shift.[60] Compared with the experimental mRIXS (Figures 4A and 4B), we can see that the CO molecules preferentially adsorbed on Pt are in the atop configuration.

Simply knowing the changes in electronic structures is not the ultimate goal. We can deduce more from these results. For example, CO as a poisoning intermediate has been extensively studied in the electro-oxidation of organic molecules, such as methanol, formic acid, and ethanol. The strong CO adsorption and active site blocking are well accepted as the primary factors causing activity decay. Based on the results illustrated in Figures 4A and 4B, the adsorbed CO might also decrease the intrinsic activity of Pt due to the altered electronic structure, which needs further study. It is also worth investigating whether the catalytic activity and Pt electronic structure can be fully restored after CO desorption. On the other hand, it is necessary to revisit the mechanisms of how the secondary metals such as Ru and Au promote the CO poisoning resistance of Pt: in addition to the well-studied promoted CO oxidation/removal and/or weakened CO adsorption, could the modulated electronic structure of Pt (e.g., through ligand or strain effects) induced by these secondary metals be a possible mechanism for the enhanced anti-poisoning property? In addressing these questions, RIXS may offer valuable information for understanding the underlying mechanisms. Specifically, RIXS can be employed to study the stability of the electronic structure in Pt-based alloy catalysts, which can facilitate an understanding of how secondary metals influence the electronic structure of Pt and, consequently, its catalytic performance and resistance to CO poisoning. Furthermore, RIXS can be utilized to investigate the electronic structure and chemical environment at the catalyst surface, thereby providing critical insights into the interactions between CO molecules and the catalyst surface.

Another instance involves Ir-based materials, where a widely accepted conclusion is that amorphous iridium oxide exhibits higher activity than rutile iridium oxide.[76] However, there is a lack of direct experimental validation regarding the electronic structure that governs the oxygen evolution reaction (OER) process in amorphous iridium oxide, leading to an incomplete understanding. In this context, Kwon et al.[24] utilized RIXS to probe the 5d orbital excitations at the iridium L_3 edge, as the electronic states associated with the OER are formed in the Ir 5d orbital.

Figures 5A and 5B display the RIXS spectra of amorphous iridium oxides prepared from two different iridium precursors: IrBL-Red synthesized from an organic precursor and IrO_x-Red

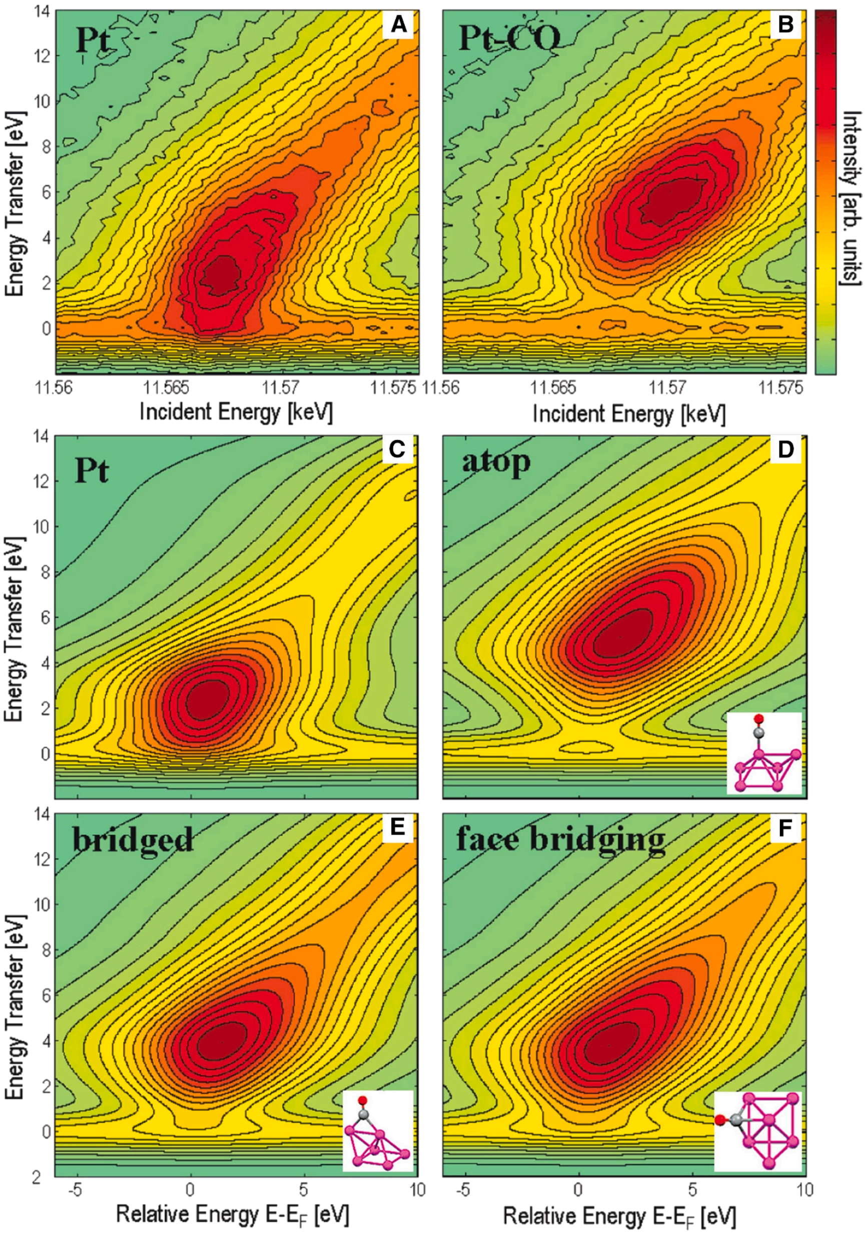

Figure 4. RIXS maps of supported Pt nanoparticles with and without CO adsorption, and theoretical comparisons

(A) Pt L_3 edge RIXS map of supported Pt nanoparticles.

(B) Pt L_3 edge RIXS map of supported Pt nanoparticles with CO adsorption.

(C–F) Theoretical RIXS maps of (C) a bare Pt_6 cluster and (D, E, and F) the cluster with adsorbed CO in three different configurations. E_F represents the Fermi level.

(A–F) Reproduced with permission.[60] Copyright 2010, American Chemical Society.

from an inorganic precursor. The RIXS spectrum of IrBL-Red shows negligible intensity below 2 eV energy loss, with a resonance peak around 3.3 eV, indicating that the Ir orbitals form σ-antibonding conduction states above the Fermi level, while fully filled π-antibonding states exist below the Fermi level, suggesting a proximity to the Ir(III) oxidation state. Additionally, the narrow excitation width reflects the limited bandwidth of the 5d orbitals. In contrast, IrO_x-Red exhibits limited scattering intensity in the low-energy loss region below 2 eV, indicating its metallic phase characteristics. The maximum intensity occurs around 3.2 eV, with a broader excitation width compared to IrBL-Red, indicating that the Ir orbitals in IrO_x-Red also form σ-antibonding conduction states above the Fermi level, but with a small number of holes in the π-symmetric states.

The integrated RIXS spectrum was obtained by summing all measured incident energy (E_i)-dependent spectra. The spectrum of IrO_2 (Figure 5C) reveals two peaks in the low-energy region below 3 eV and a broad asymmetric peak in the high-energy region. Density functional theory (DFT) calculations (Figure 5D) indicate that the π anti-bonding states are predominantly occupied and that there is a hole state crossing the Fermi level. The excitation widths of IrBL-Red (Figure 5E) and IrO_x-Red (Figure 5F) in the high-energy region are significantly smaller than that of IrO_2, reflecting a narrower bandwidth of the 5d orbitals, likely due to the lack of translational periodicity in the nanostructure, larger Ir-O bond lengths, and lower structural symmetry.

The authors propose that the large crystal field and orbital overlap of the Ir 5d orbitals in IrBL-Red and IrO_x-Red are key factors determining the states of the Ir 5d orbitals in these materials. Structural details further contribute to significant differences in their orbital states. The distinct electronic and atomic structures of IrBL-Red and IrO_x-Red under oxidative conditions result in varying OER activities. However, reliable comparisons of OER activity require detailed investigations of the active surface sites and areas, which presents a challenge in amorphous catalysts. Therefore, future *in situ*/operando studies to monitor the evolution of electronic and atomic structures will be particularly critical for elucidating structure-activity relationships.

RIXS IN MONITORING CHANGES IN ELECTRONIC STRUCTURE DURING THE REDOX PROCESS

In addition to the electronic structure itself, the changes in electronic structure have greater relevance to the reaction and degradation mechanisms, which thus attract more attention.[6,10,15,33,34,71,77–89] With the advancement of third-generation synchrotron radiation sources, the brightness and

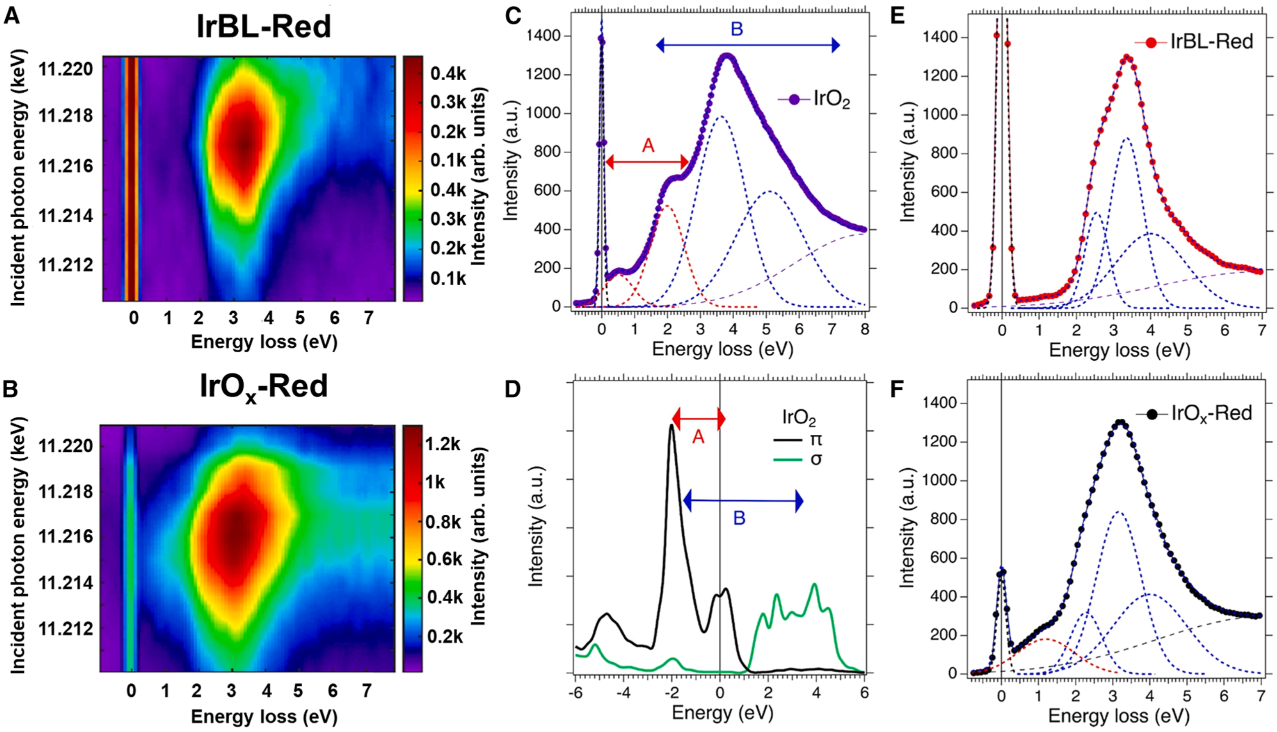

Figure 5. RIXS spectra and DFT calculations of different iridium-based materials

(A and B) RIXS spectra vs. E_i of IrBL-Red and IrO_x-Red. IrBL-Red: The maximum intensity is located around 3.4 eV. There is no clear intensity below 2 eV. IrO_x-Red: The maximum intensity is located around 3.2 eV. The low energy loss region below 2 eV shows a finite scattering intensity.

(C) RIXS spectra of IrO_2 (Rutile). The low-energy region below 3 eV (indicated by A, red font) is fitted with two peaks at around 0.5 and 2 eV, and the high-energy region above 3 eV (indicated by B, blue font) is fitted with two peaks at around 3.7 and 5.3 eV.

(D) DFT calculations of the 5d orbitals for IrO_2. The excitations in the A region (red font) originate from excitations within the π states. The transitions from π to σ states contribute to the B region (bule font) excitations.

(E and F) The high-energy excitations in IrBL-Red and IrO_x-Red fitted with three Gaussian functions. One broad Gaussian function is added to describe the broad low-energy excitation in IrO_x-Red.

(A–F) Reproduced with permission.[24] Copyright 2021, American Chemical Society.

photon detection efficiency of RIXS technique have been significantly enhanced. Furthermore, the development of high-efficiency spectrometers has enabled mRIXS to acquire data across a broad working energy range of up to 1500 eV within shorter data acquisition times.[29] These advancements have propelled the development of *in situ*/operando RIXS in probing electronic structure changes.

Figure 6A demonstrates the design of a flow cell for *in situ* RIXS investigations, which is used to study the reaction mechanisms of MnO_x catalyst toward OER in 0.1 M borate buffer electrolyte.[78] The Mn element belongs to the 1st line of d-block metals, which has gradually gained prominence in catalysis and batteries. Nine potential points were selected based on the potential cycling curves (Figure 6B) to investigate the structural transformations at different OER stages. Figure 6C presents the XAS curves at the Mn L_3 and L_2 edges of the MnO_x catalyst at different OER stages. It can be seen that the Mn L_3 peaks related to Mn^{III} are suppressed while the peaks for Mn^{IV} are enhanced by increasing the OER potential from 0.75 to 1.45 V. Meanwhile, the Mn L_2 edge generally positively shifts as the potential increases, which is consistent with the increasing oxidation state of Mn at higher potentials. Notably, within this potential range, the OER does not take place yet. Based on Figure 6C, it appears that the oxidation state of MnO_x does not significantly change above 1.45 V until the OER begins at 1.6 V (Figure 6B). Therefore, it is intriguing to investigate what occurs on the catalyst between 1.45 and 1.6 V.

The *in situ* RIXS in Figure 6D can provide more information beyond XAS. The investigated incident energies are selected based on Figure 6C. If we look at the *in situ* RIXS curves at each incident energy, it can be found that the peak positions are independent of the applied potential. Moreover, the peaks related to d-d transitions and charge transfer rarely change at increased incident energy. These results indicate that the required energy to trigger d-d transitions and charge transfer is similar for different Mn oxidation states. That is to say, increasing the applied potential has a negligible effect on the band gap. On the other hand, interestingly, the peak intensity, especially for charge transfer collected at Mn L_3 edge, is significantly increased by 8%–10% along with the increased potential from 1.45 V to above 1.75 V (right inset of Figure 6D). This implies that the charge transfer takes place at > 1.45 V, although the oxidation state does not change in this potential range (Figure 6C).

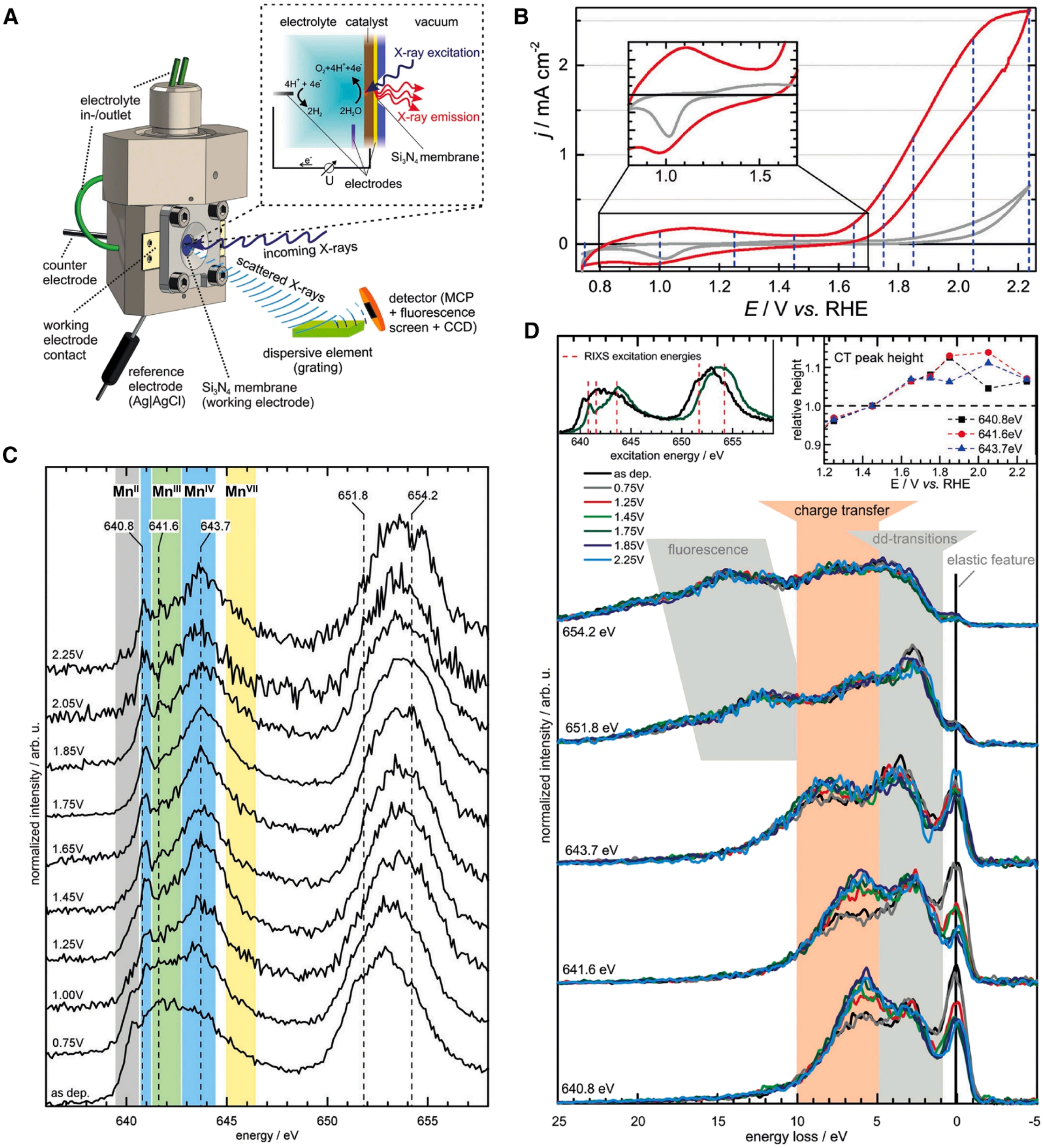

Figure 6. *In-situ* characterization of MnO_x catalyst via XAS and RIXS in an electrochemical flow cell

(A) An illustration of the flow cell for the *in-situ* XAS and RIXS experiments.

(B) Cyclic voltammograms curves in 0.1 M borate buffer solution (pH = 9.2) for the electrodeposited MnO_x catalyst on the substrate (red) and the Au/Si_3N_4 substrate (gray).

(C) *In-situ* sXAS-PFY at Mn L_2 and L_3 edge for MnO_x in 0.1 M borate buffer solution (pH = 9.2) with no applied potential (as dep.) and at different applied potentials. The dash lines represent the incident energies to perform RIXS. Backgrounds show the regions corresponding to the specific oxidation state of Mn.

(D) In-situ RIXS for MnO_x in 0.1 M borate buffer solution (pH = 9.2) with no applied potential (as dep.) and at different applied potentials. The typical features are highlighted by the colored backgrounds.

(A–D) Reproduced with permission.[78] Copyright 2019, Wiley-VCH.

By combining the XAS and RIXS results, some conclusions can be achieved in understanding the electronic structure change for MnO_x catalyst during OER operation: 1) +4 is the highest oxidation state for Mn involved in OER; 2) the oxidation of MnO_x is completed before 1.45 V and is not directly involved in OER; 3) the charge transfer (from O to Mn) is necessary for OER which requires potential higher than 1.75 V.

The above example uses RIXS with soft X-rays to investigate the electronic structure change at Mn L edges. Accordingly, the RIXS can also be conducted using hard X-rays, e.g., studying

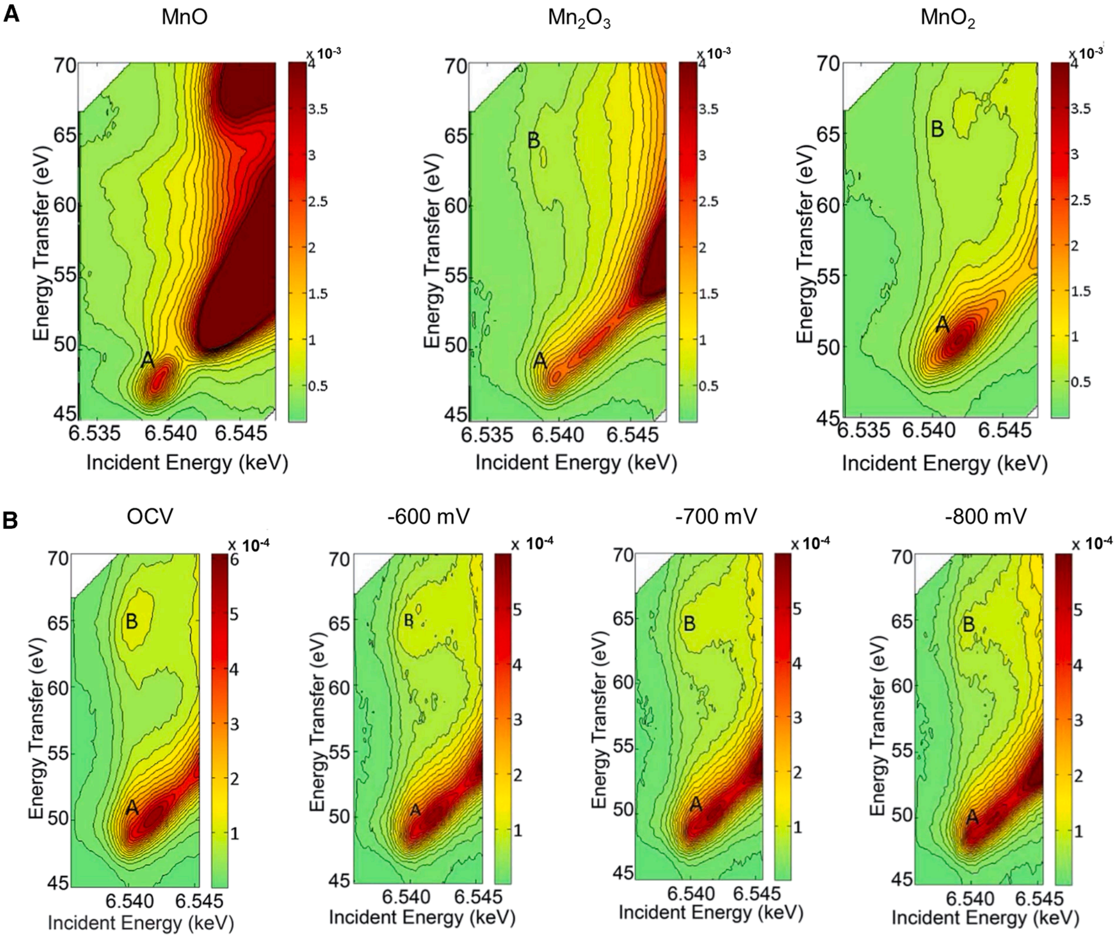

Figure 7. RIXS analysis of Mn oxidation states in reference samples and *in-situ* LSM50 electrode at various potentials

(A) Mn K edge RIXS maps for the three reference samples including MnO (Mn^{2+}), Mn$_2$O$_3$ (Mn^{3+}), and MnO$_2$ (Mn^{4+}).

(B) *In-situ* RIXS maps for LSM50 electrode at 500°C in the air at OCV, −600 mV, −700 mV and −800 mV.

(A) and (B) Reproduced from ref. [90] Open Access article.

the Mn K edge. As illustrated in ref. [90], the (La$_{0.5}$Sr$_{0.5}$)$_{0.99}$MnO$_{3-\beta}$ (denoted as LSM50) as the electrode is investigated at 500°C for electrochemical cathodic polarization. As shown in Figure 7A, the RIXS maps around the Mn K edge for the reference samples including MnO, Mn$_2$O$_3$, and MnO$_2$ have two typical regions: one is marked as A, which represents the 1s spin-down transition to 3d and another B region means the spin-up transition. Particularly, the reference MnO does not demonstrate the typical B region, which is likely due to the occupied high-spin electrons in all the 3d orbitals for Mn^{2+}. Consequently, only spin-down transitions are permitted, while the region B representing spin-up transitions is forbidden. Inversely, one or more empty orbitals are in the Mn ions with higher oxidation states such as Mn^{3+} and Mn^{4+}, so that both spin-up and spin-down could take place in Mn$_2$O$_3$ and MnO$_2$.

Based on the database for the reference MnO$_x$ samples, the *in situ* RIXS of the LSM electrode presents both regions A (spin-down) and B (spin-up) at OCV. As the cathodic overpotential increases, the signal for region B is suppressed. Such a potential-related electronic structure change is attributed to the reduced Mn oxidation state (e.g., from 3d^3 to 3d^4; no Mn^{2+} with 3d^5 configuration is formed in this work) at high cathodic overpotential and the decreased number of spin-up transitions. In addition to Mn elements, the RIXS is also helpful to investigate the evolution of electronic structures for other TMs such as Ni and Co.[7,13,14,91,92]

As mentioned above, studying the light elements such as O and N is challenging by XAS, which, fortunately, can be well investigated by RIXS.[6,33,34,57,62,77,88,93–96] Understanding the electronic structure change of oxygen is extremely important for Li-ion batteries. For example, the layered lithium-TM oxides, e.g., LiCoO$_2$,[97] have been intensively investigated and widely used as cathode materials for Li-ion batteries due to the high theoretical capacity (274 mAh g^{-1}), conductivity, and density. However, its practical discharge capacity, while maintaining an acceptable level of cycle reversibility, is only ∼173 mAh g^{-1} (Li$_{1-x}$CoO$_2$, x = ∼ 0.63; 4.45 V versus Li/Li$^+$). Increasing the charge cut-off voltage is a promising strategy to enhance the capacity, as demonstrated by the increase to ∼185 mAh g^{-1} at 4.5 V versus Li/Li$^+$ and ∼220 mAh g^{-1} at 4.6 V versus Li/Li$^+$.

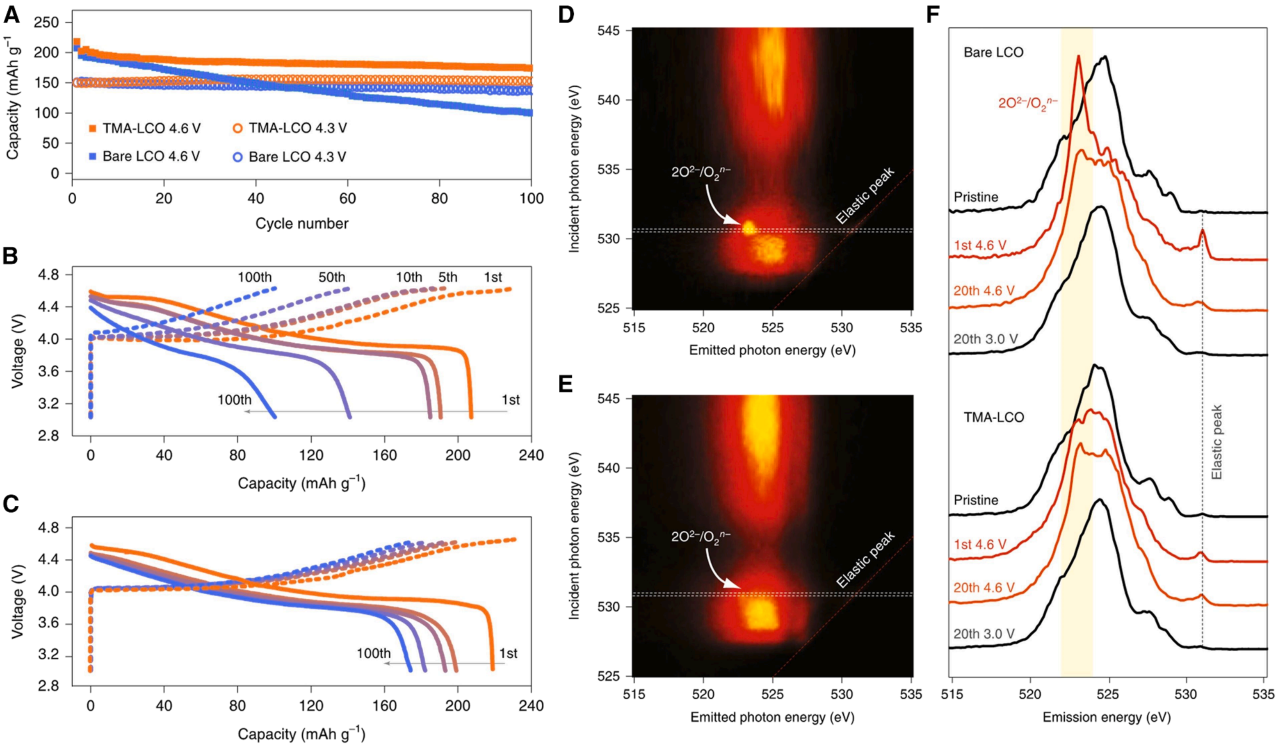

Figure 8. Cycle performance, charge-discharge curves, and RIXS analysis of bare LCO and TMA-LCO half cells

(A) Comparison of cycle performances using half cells with bare LCO and TMA-LCO.

(B and C) The charge-discharge curves of half cells with (B) bare LCO and (C) TMA-LCO at the 1st, 5th, 10th, 50th, and 100th cycle.

(D and E) O K edge mRIXS for (D) bare LCO and (E) TMA-LCO charged at 4.6 V.

(F) RIXS spectra for bare LCO and TMA-LCO at different stages including the pristine state, 4.6 V charged states, and the 3.0 V discharged state after the 20th cycle with an X-ray excitation energy of 531 eV.

(A–F) Reproduced with permission.[79] Copyright 2019, Springer Nature.

However, a higher cut-off voltage adversely leads to fast degradation. It is thus important to monitor the degradation mechanisms and develop advanced stable materials for Li-ion batteries.

Recent progress demonstrated that $LiCoO_2$ (LCO) doped by trace Ti-Mg-Al (denoted as TMA-LCO) presented excellent cycling stability at 4.6 V versus Li/Li^+.[79] As shown in Figures 8A–8C, the stability for bare LCO and TMA-LCO is similar if the cut-off voltage is set as 4.3 V. Not surprisingly, once the cut-off voltage is selected up to 4.6 V, although the initial capacity is increased, the stability for bare LCO deteriorates significantly. For TMA-LCO, its stability at a cut-off voltage of 4.6 V is superior, maintaining a capacity of 174 mAh g^{-1} after 100 cycles at 0.5 C. In addition, the capacity for full LCO/graphite and TMA-LCO/graphite pouch cells are 51.3 mAh g^{-1} and 178.2 mAh g^{-1}, respectively, after 70 cycles (not presented in Figure 8), confirming the stability of TMA-LCO cathode material for Li-ion battery.

The improved stability can be partially due to the suppressed oxygen redox reaction in TMA-LCO, which is confirmed by RIXS investigations. The RIXS is employed because the conventional XAS at the O K edge has limitations in resolving lattice oxygen contributions due to strong metal 3d-oxygen 2p hybridization. As shown in Figure 8D, the O K edge mRIXS of bare LCO presents an obvious isolated point, representing the oxidation of O^{2-} at a deeply delithiated state. In contrast, such a feature cannot be observed for the TMA-LCO (Figure 8E). Considering the probing depth for RIXS is ~150 nm, this phenomenon supports that the oxygen redox rarely happens in the outer shell of TMA-LCO. The stable oxygen contributes to the overall battery stability at a high voltage of up to 4.6 V. Even after 20 cycles, the TMA-LCO demonstrates significantly better oxygen stability than bare LCO, as shown in Figure 8F. This indicates that the oxygen redox reaction is a key factor that affects the cycling stability of the layered oxide cathode materials, which is consistent with other reports and can be well studied by RIXS.[32–34,71,95,98–101]

In recent years, high-resolution RIXS has been successfully employed to study the vibrational spectra of molecular species in energy materials, revealing the dynamic evolution of molecular species during the cycling process of energy materials.[32–34,61,84,86,88,89,96,102–105] A representative example is the oxygen redox process in lithium-ion battery electrodes. Combined O K edge XAS and RIXS studies on $Li_x[Ni_{0.65}Co_{0.25}Mn_{0.1}]O_2$ (Figure 9A) reveal that as lithium ions are extracted ($x < 0.75$), the integrated intensity under the O K spectral peak increases significantly, confirming the formation of oxygen hole states (O^-). Simultaneously, a new RIXS excitation feature at an emission energy of ~56.5 eV provides direct spectroscopic

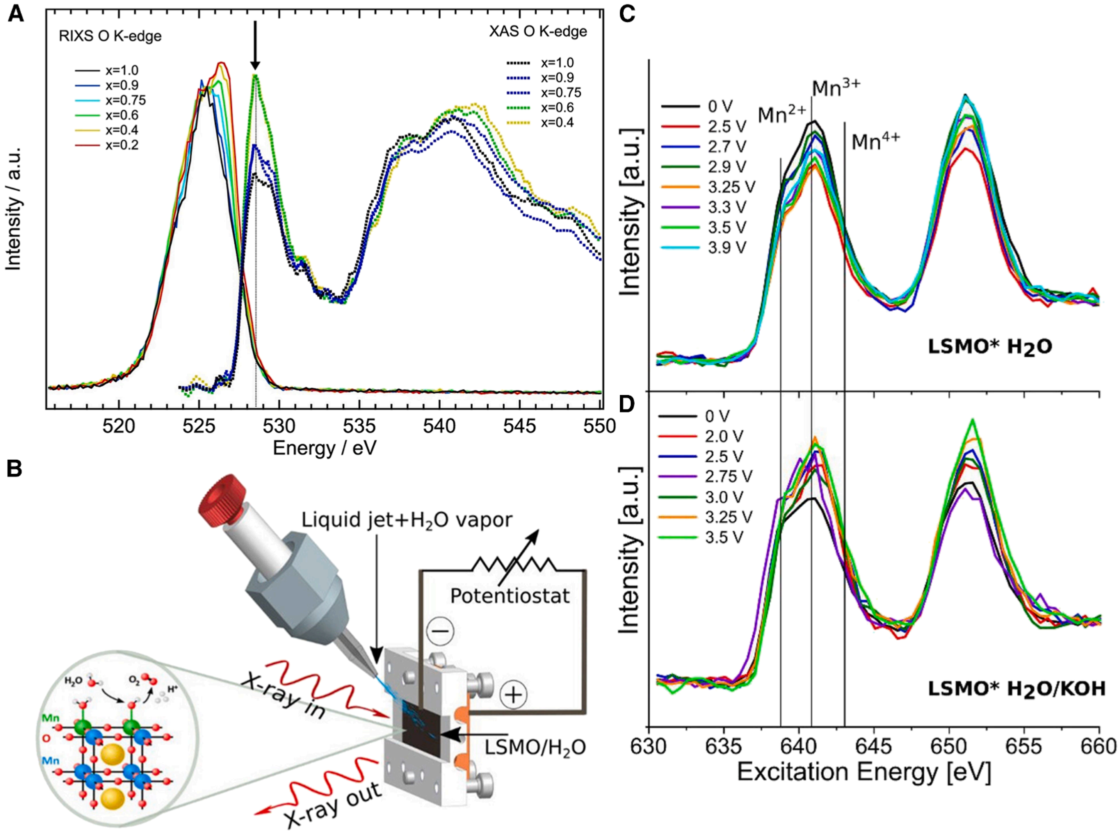

Figure 9. X-ray spectroscopy analysis of O and Mn redox behavior of electrode materials and design of liquid jet coupling system
(A) O K edge RIXS and XAS spectra (TFY mode) of $Li_x[Ni_{0.65}Co_{0.25}Mn_{0.1}]O_2$ excited at the peak of the absorption resonance (indicated by the arrow).
(B) Schematic diagram of the coupling system between liquid jet and X-ray spectrometer.
(C) *In-situ* Mn L edge iPFY of LSMO*H_2O for varying voltages.
(D) *In-situ* Mn L edge iPFY of LSMO*H_2O/KOH for varying voltages.
(A) Reproduced form ref. [61] Copyright 2017, Elsevier.
(B–D) Reproduced form ref. [106] Open Access article.

evidence for oxygen participation in charge compensation. Notably, the emergence of new electronic states in the O 2p band and their progressive enhancement during delithiation reflect the reconstruction of oxygen electronic states from a single hybridized configuration to competitive multi-state coupling. This oxygen-involved redox mechanism offers a novel pathway to transcend the capacity limits of conventional electrode materials and establishes critical theoretical connections between battery reaction kinetics and capacity degradation mechanisms.

However, oxygen evolution pathways may exhibit significant material dependence. For instance, Hu et al.[84] demonstrated that while $LiCoO_2$ undergoes oxygen charge compensation and O-O bond shortening during delithiation, it does not form $(O_2)^{n-}$ dimers or release gas—a stark contrast to the pronounced O-O bond formation in Li-rich Li_2RuO_3. This divergence highlights the regulatory role of local coordination environments on oxygen reaction pathways. Recently, Hirsbrunner et al.[86] identified a novel vibrational RIXS feature in the O K pre-edge region (>533 eV) for two cathode materials, $Li_xNi_{0.90}Co_{0.05}Al_{0.05}O_2$ (NCA) and $Li_{1.2}Ni_{0.13}Co_{0.13}Mn_{0.54}O_2$ (LRNMC), attributed to hydroxyl (OH^-) group formation. Nevertheless, the precise bonding sites and accumulation pathways require further investigation.

Similarly, recent studies have expanded the application of RIXS to probe chemical reaction dynamics, despite the stringent resolution requirements imposed on spectrometers.[87,106–108] Reuss and colleagues[106] have constructed a coupled system integrating a liquid jet with an X-ray spectrometer (Figure 9B) to monitor the changes in the oxidation state of Mn at the surface of $La_{0.6}Sr_{0.4}MnO_3$ (LSMO) in both aqueous (LSMO*H_2O) and alkaline (LSMO*H_2O/KOH) environments during reactions. Leveraging the megahertz sample exchange frequency enabled by the liquid jet technique, high-resolution monitoring was achieved. For LSMO*H_2O, as the voltage increased from 0 to 3.9 V, the intensity of the first transition band (639–643 eV) in the iPFY spectrum decreased, while the intensity of the second transition band (peaking at 652.5 eV) increased (Figure 9C). This variation indicates a change in the Mn oxidation state at the LSMO surface with increasing voltage, potentially transitioning from a higher $Mn^{3+/4+}$ mixed-valent state to a lower Mn^{3+} or $Mn^{2+/3+}$ mixed-valent state. In contrast, for LSMO*H_2O/KOH, the iPFY spectrum at 0 V resembled that of LSMO*H_2O. However, as the voltage increased, an enhancement in the low-energy transition shoulder of the *in situ* iPFY spectrum was observed, exhibiting similar spectral evolution to LSMO*H_2O during voltage scanning (Figure 9D). This suggests that, in the presence of alkaline solution, the application of voltage also induces changes in the Mn oxidation state at the LSMO surface, resulting in the formation of a lower $Mn^{2+/3+}$ mixed-valent state. Notably, the Mn variations in the two systems differ, potentially due to alterations in the chemical environment and electronic structure at the LSMO surface induced by the alkaline solution. These findings support the notion that, under more realistic oxidation conditions, the LSMO-catalyzed OER involves dynamic Mn redox cycling between multiple oxidation states. Consequently, there remains a pressing need for further development of *in situ* characterization devices or methodologies to capture the evolution of catalyst electronic structures with greater precision and under conditions that more closely mirror actual reaction environments.

RIXS IN QUANTITATIVE ANALYSIS

Quantification is another unique application of RIXS.[57,62,109–112] Quantification is important in understanding energy conversion and storage applications. For example, in addition to the stability effects as discussed in Figure 10, it has been proposed that the oxygen redox reaction in $LiNi_xCo_yMn_zO_2$ oxide (can be regarded as a derivative from $LiCoO_2$) cathodes significantly contributed to the enhanced capacity during lithium-ion battery charging and discharging.[110] In this regard, the redox reaction of lattice oxygen is of significance in improving the capacity, working voltage, and cycling lifetime.

Dai et al.[110] quantified the redox reactions of both Mn and lattice oxygen in $Na_{2/3}Mg_{1/3}Mn_{2/3}O_2$ for Na-ion battery. The electrochemical charging and discharging curves for $Na_{2/3}Mg_{1/3}Mn_{2/3}O_2$ at 0.1 C are shown in Figure 10A, where the indicated points at different stages are tested by RIXS. Figure 10B presents the O K edge mRIXS for the electrodes at different states of charge during the initial charge and discharge. The features at an emission energy of ~525 eV are attributed to the O^{2-} states in typical TM oxides while that at 523.7 eV is associated with the oxygen redox reaction, which appears only if the potential reaches 4.2 V and becomes stronger if further charging. Inversely, this feature gradually weakens and disappears when the potential is below 2.5 V. Figure 10C demonstrates the super-partial fluorescence yield analysis (sPFY) of the emission energy feature at 523.7 eV, which is extracted from mRIXS. The main changes are at the excitation energy of 531 eV, which emerges after the charge plateau, reaches the top at the fully charged state, and then decreases. By combining the RIXS information of O K edge and Mn L edge, the quantification of Mn redox and O redox can be conducted as shown in Figure 10D, where the reversibility of lattice O redox in the initial cycle is calculated as 79%.

Similarly, such a RIXS-based strategy is applicable to investigate the contribution and reversibility of lattice oxygen redox to the battery cycling performance after different cycles. The results support that the O redox activities are stable after 50 cycles and are maintained at 87% after 100 cycles. The above results and discussion are based on the $Na_{2/3}Mg_{1/3}Mn_{2/3}O_2$ electrode for the Na-ion battery. Similar RIXS-based approaches have been extended to Li-ion battery materials, such as $Li_{1.17}Ni_{0.21}Co_{0.08}Mn_{0.54}O_2$.[110]

RIXS is also applicable for studying materials beyond metal oxides: it can be used to track and quantify the change of occupied 3d states in the metal chalcogenides, e.g., VS_4, which has a superior theoretical capacity of 1196 mAh g^{-1} (assuming complete reaction from VS_4 to Li_2S) and is therefore promising for Li-ion battery applications. As shown in Figure 11A, the mRIXS of pristine VS_4 exhibits a typical parallel line to the elastic line, representing the d-d excitations.[113] Intensity of the d-d excitations is related to the hybridization strength of V 3d-S 3p. Remarkably, the d-d excitations feature decreases in intensity after discharge to 1.0 V (Figure 11B) compared to that of the pristine VS_4. Further, it can hardly be observed when discharge to 0.05 V (Figure 11C); meanwhile, the d-d excitation recovers after charging (Figures 11D and 11E). Similar trends are also observed in the following cycles (Figures 11F-11I).

Besides, the features at emission energy of 514.5 eV and 517 eV correspond to V 3d-S 3p hybridization and pure V 3d states, respectively. These two properties are dependent on the charge and discharge states. As shown in Figures 11B-11E, the V 3d-S 3p hybridization decreases along with the discharge process (Figures 11B and 11C); while the pure V 3d becomes dominant along with the discharge process. During the subsequent charge cycle, the V 3d-S 3p state reappears, while the intensity of pure V 3d state diminishes (Figures 11D and 11E). Similar trends are observed in the following cycles (Figures 11F-11I). By plotting the intensity ratio of V 3d-S 3p to pure V 3d vs. the charge and discharge time, the quantification of the hybridization strength of V and S can be viewed as shown in Figure 11J. It is quite clear that the V-S hybridization decreases during discharge due to the conversion of VS_4 to Li_2S and metallic V, which then increases during the subsequent charge process, indicating the partially reversible intercalation and VS_4 conversion reaction. Similarly, the related intensity ratio *vs.* cycle number can be plotted as shown in Figure 11K. For all the charged states, the ratio does not change much, in contrast to the significant changes for the discharged states for different cycles. These results support that the charged products after different cycles are similar while those for discharged products are quite different. After 10 cycles, the reversibility of the reactions and capacity remarkably decreases.

Another interesting application of RIXS in quantification is to monitor the concentration change of an electrode. For example, in Li-S batteries, the mechanisms of lithium polysulfide formation and the related reaction with host and electrolyte during discharge are important.[114] As shown in Figure 12A, the mRIXS of the representative Li_2S_4 presents two typical excitation energies: the one at 2470.7 eV represents the pre-edge (S and Li_2S_x); another one at 2473.0 eV is attributed to the contribution of Li_2S from S and Li_2S_x. These two excitation energies were used to quantify the relative amount of Li_2S_x and Li_2S based on the linear combination fit and database of reference samples. As shown in Figure 12B, the *in situ* RIXS curves at lithium polysulfide pre-edge (i.e., 2470.7 eV) at different discharge states are conducted. The curves can be deconvoluted into S (blue) and Li_2S_x (red). Meanwhile, another set of RIXS at 2473 eV in

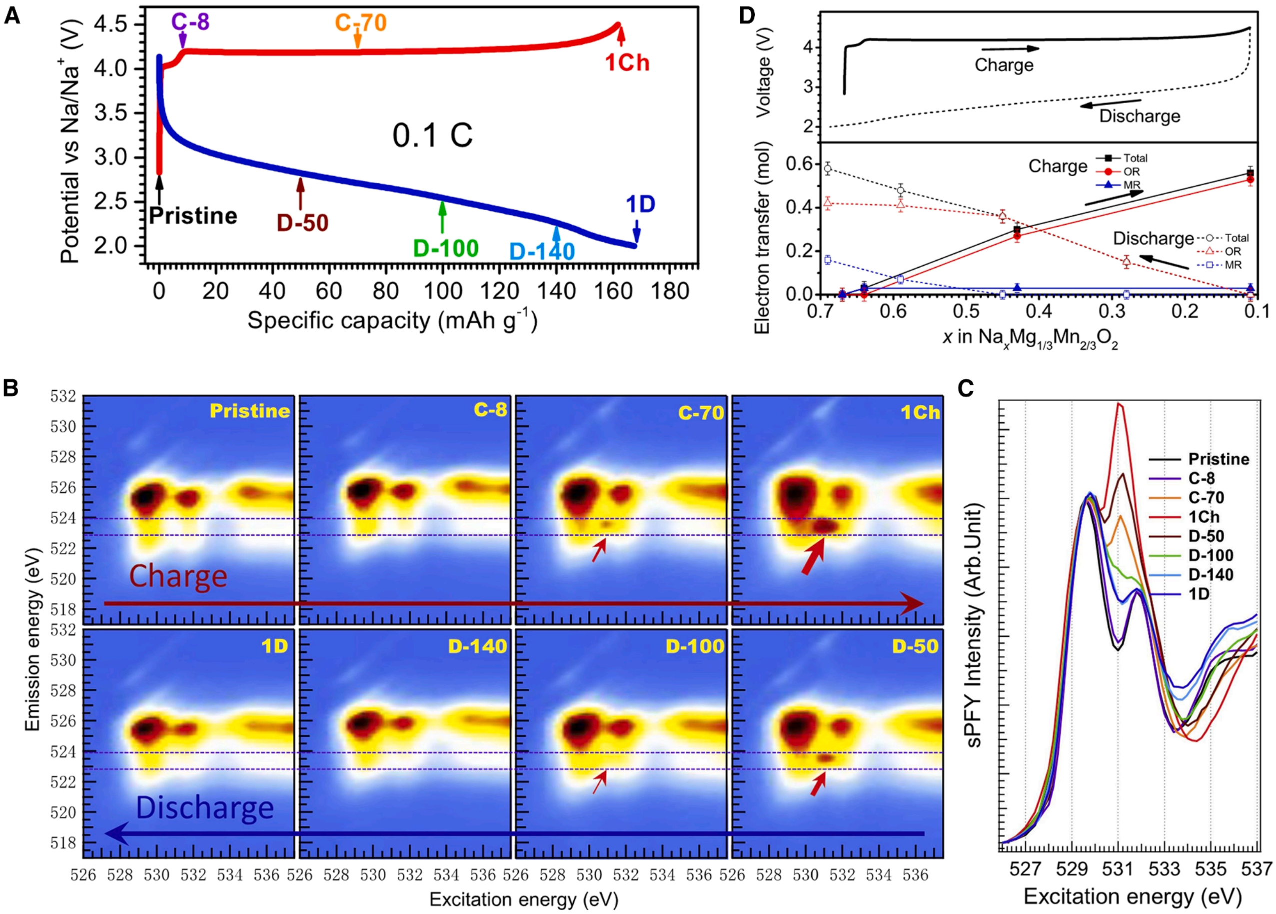

Figure 10. Charge-discharge profiles and RIXS analysis of $Na_{2/3}Mg_{1/3}Mn_{2/3}O_2$ electrode redox reactions

(A) The initial charge and discharge curves of the $Na_{2/3}Mg_{1/3}Mn_{2/3}O_2$ electrode at 0.1 C. The charge and discharge states for the RIXS study are named and marked with arrows.

(B) The mRIXS of $Na_{2/3}Mg_{1/3}Mn_{2/3}O_2$ electrodes at different charge and discharge states as indicated in Figure 10A. The key O redox feature is indicated by the red arrows.

(C) sPFY spectra extracted from mRIXS by integrating the characteristic 523.7 eV emission-energy range, as indicated by the horizontal purple dashed lines in Figure 10B.

(D) Contribution of O redox during charging and discharging, assuming a linear relationship between the amount of O redox and the peak area at 531 eV of sPFY curves.

(A–D) Reproduced with permission.[110] Copyright 2018, Elsevier.

excitation energy is conducted and shown in Figure 12C, which consists of the S + Li_2S_x (blue) and Li_2S (red). Based on the fitting results, the relative amounts of S, Li_2S_x, and Li_2S can be plotted against the discharging process (Figure 12D).

SUMMARY AND PERSPECTIVE

The electronic structures of TMs and light elements have attracted wide attention for the research and development of renewable energy conversion and storage applications. This is because these elements play key roles in determining the kinetics of chemical reactions involved in batteries, fuel cells, and electrolyzers. Traditional experimental techniques, such as XPS and XAS, have been well accepted as powerful tools to study their electronic structures, but these still suffer from some limitations. As such, the emerging RIXS technique, itself a combination of X-ray absorption and emission spectroscopies, can provide comprehensive information for both occupied and unoccupied orbitals, shedding light into the electronic structures of TM and light elements. In this review, we briefly introduce the applications of RIXS in understanding the electronic structure, monitoring the changes of the electronic structure during the energy conversion and storage process, as well as the quantitative analysis of different features. The purpose of this paper is to trigger the interest of using RIXS in material study for renewable energy conversion and storage applications. However, the appeal of RIXS is not limited to electronic structure alone, as it can be also used for solid/liquid or solid/gas interface analysis of materials and energy storage systems,[40,52,62,85,94,115] probing bandgap transitions and electronic correlations of the material system in semiconductors for photo-involved industries, and so on.[72,116]

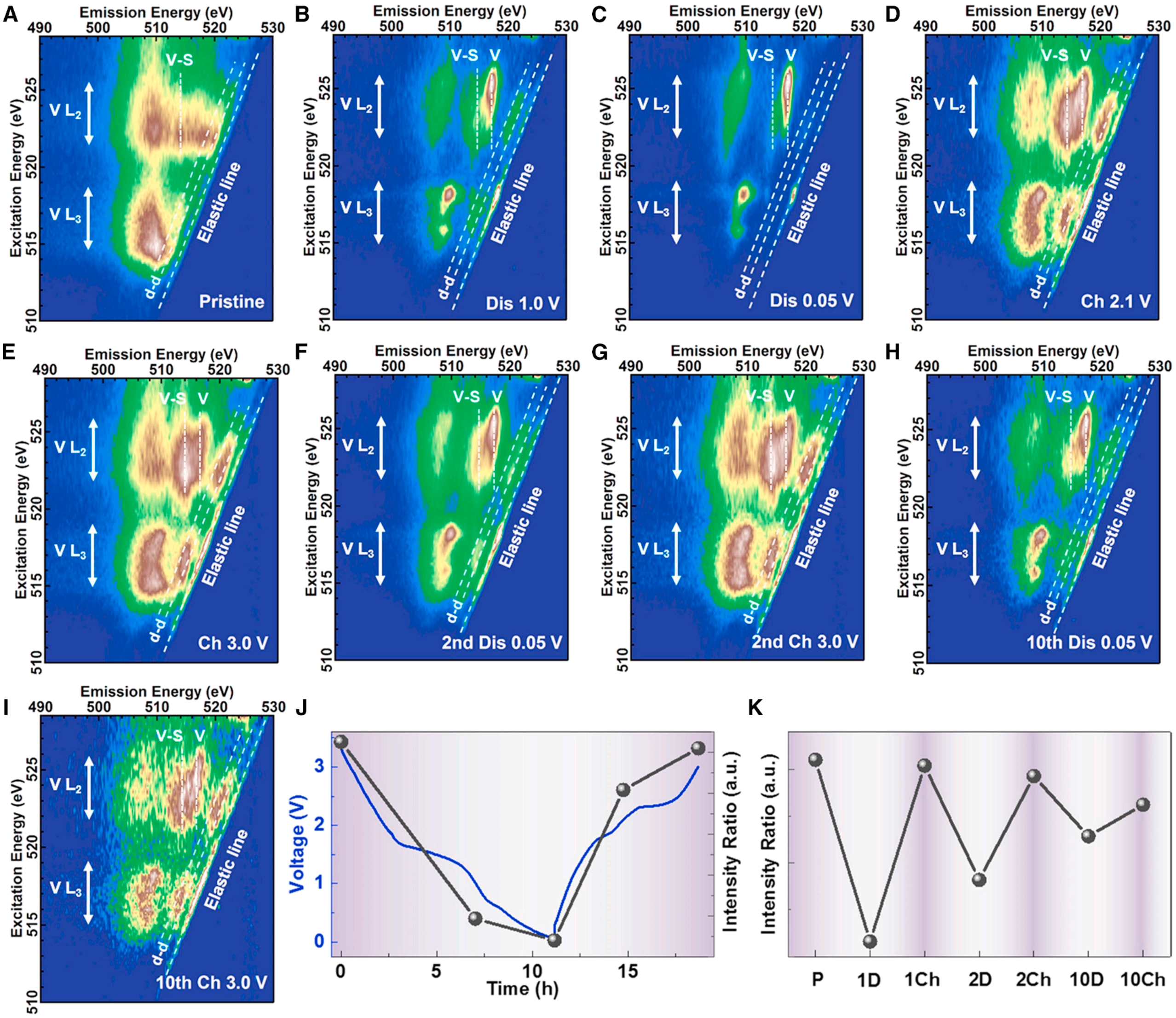

Figure 11. RIXS analysis of VS_4 electrode at various charge-discharge states and cycle numbers

(A–I) V L edge mRIXS of VS_4 electrode at different charge and discharge states. The mRIXS for the pristine electrode was measured using VS_4 without any electrochemical processes.

(J and K) Intensity ratio change of the V 3d-S 3p hybridized states to the pure V 3d states as a function of (J) state of charge and (K) cycle number.

(A–K) Reproduced with permission.[111] Copyright 2018, Elsevier.

A lot of people have carried out XAS/XES,[117–124] X-ray reflectivity experiments,[125–128] and XPS.[129] We should note that RIXS is not well known by the community in energy conversion and storage as there is not much work yet using RIXS in studying energy conversion and storage applications such as batteries, fuel cells, and electrolyzers. This is likely because the conducting of RIXS experiments highly relies on the limited synchrotron light sources (RIXS is essentially a photon-hungry technique),[130] as well as the increasing demand to comprehensively and deeply understand the reaction and degradation mechanisms of key materials for energy conversion and storage devices in recent years. To extend the application range of RIXS, the developments of high flux density, even next-generation synchrotron light sources, and more advanced beamline end stations are necessary.

With the construction of more beamlines for RIXS experiments and its increasing application in future research, an integrated RIXS database encompassing various materials in renewable energy conversion and storage will be established. This database will serve as a valuable resource for the scientific community, facilitating comprehensive analysis and comparison of RIXS data across different materials and systems. We believe scientists will gain a deeper understanding of this technique, driving its widespread adoption in the fields of energy conversion and storage. Here, a list of global RIXS facilities is provided in Table 1 referring to the publication by Groot

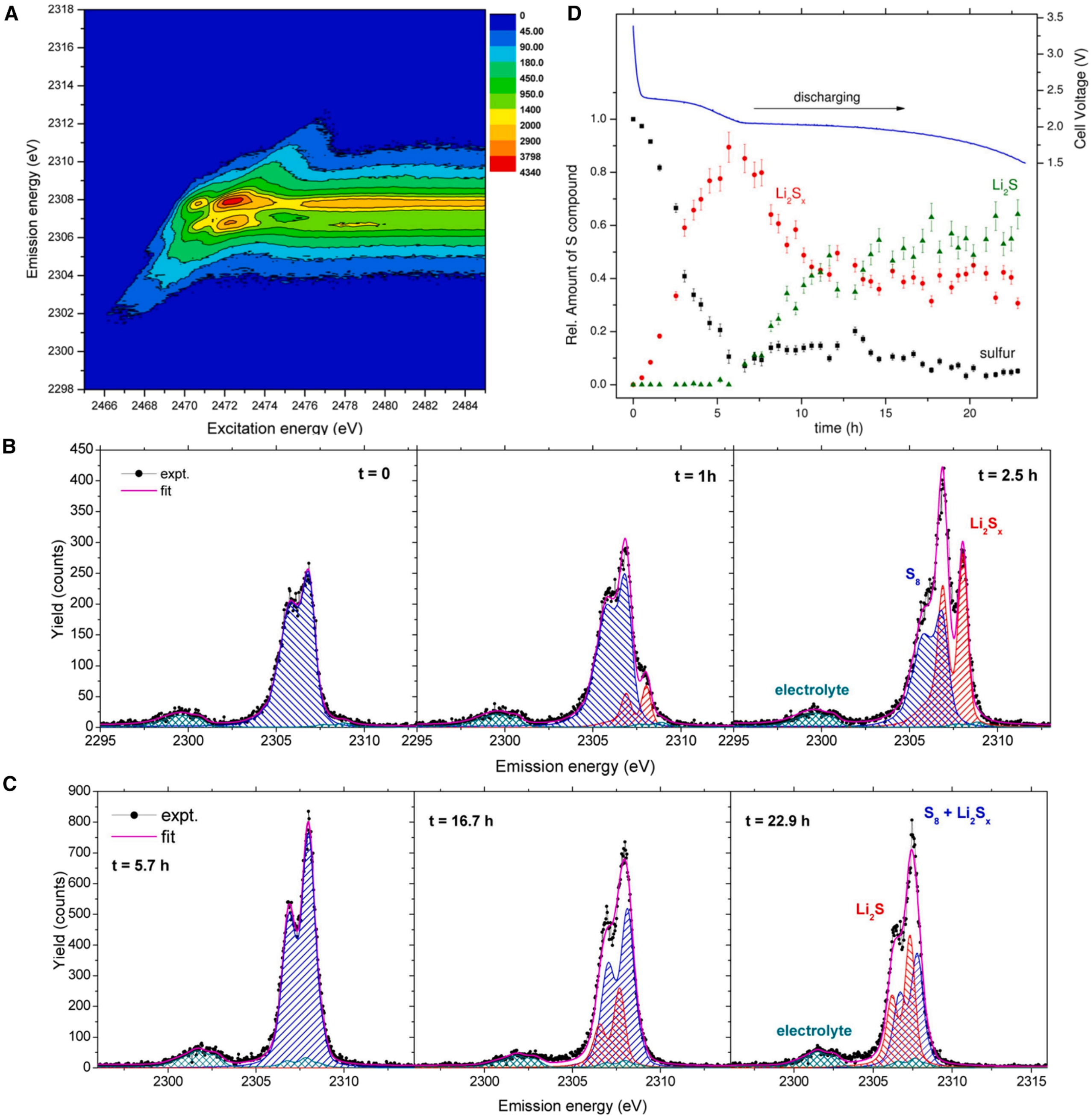

Figure 12. RIXS analysis and discharge curve of Li-S battery with evolution of cathode components

(A) The RIXS map for the typical Li_2S_4.

(B and C) The operando sulfur RXES spectra at the excitation energy of (B) 2470.7 eV and (C) 2473 eV using a Li-S battery at the beginning of the discharge process.

(D) The discharge curve of the Li-S cell, together with the evolution of relative intensity ratios of sulfur, Li_2S_x and Li_2S within the battery cathode during the discharge process.

(A–D) Reproduced with permission.[112] Copyright 2016, American Chemical Society.

et al.,[131] and their key parameters are summarized for reference.

Beyond the expansion of the RIXS database, future research may also explore synergies with advanced analytics (e.g., machine learning). While machine learning is not a necessity, it does offer a potentially beneficial tool for analyzing and interpreting RIXS data more efficiently and accurately. By leveraging advanced algorithms and computational techniques, machine

Table 1. RIXS facilities and corresponding beamline parameters

Synchrotron	Beamline/Station		Energy range	Resolution/Resolving power (RP)
European Synchrotron Radiation Facility (ESRF), Grenoble, France	ID20		4–20 keV	25 meV–2 eV
	ID26		2.4–27 keV	–
	ID32		0.3–1.6 keV	aim combined RP: 30000
	BM20 (ROBL)		2.8–36 keV; 3–20 keV for XES or RIXS	high energy resolution
	BM30 (FAME)[132]		Si (220): 5–40 keV	$\Delta E/E$: $\sim 5.6 \times 10^{-6}$ for Si (220)
SOLEIL, Saclay, France	GALAXIES		2.3–12 keV	ΔE@8 keV: 100 meV–1 eV
	MARS		3.5–36 keV; 3.5–21 keV for focused beam	$\Delta E/E$: $<3 \times 10^{-4}$
	SEXTANTS		50–1700 eV; optimized: 70–1500 eV	$E/\Delta E$: $>1 \times 10^{4}$ up to 1200 eV
MAX-IV, Lund, Sweden	SPECIES		30–1500 eV	RP up to 10000 (at N edge)
	VERITAS		250 -1500 eV	currently 15000, new optics to be installed
European XFEL, Hamburg, Germany	SCS	hRIXS	0.26–3 keV; 0.4–1.4 keV for hRIXS	combined RP (monochromator & hRIXS): up to 10000 (high resolution), up to 3000 (low resolution)
BESSY II, Berlin, Germany	UE52_SGM	AXSYS TES	100–1500 eV	$E/\Delta E$: >4000
	UE51_PGM-1; UE51_PGM-2	LiXEdrom	under construction	
	U41 SGM	METRIXS	250–1000 eV	–
	UE112_PGM-1	meV RIXS	8–690 eV	$E/\Delta E$: 30000 (20–150 eV); $E/\Delta E$: >20000 (150–350 eV)
	U41	PEAXIS	200–1200 eV	$E/\Delta E$@400 eV: 6500–14000; $E/\Delta E$@867 eV: 5500–12500
	PM2	VEKMAG	20–1600 eV	Variable
Karlsruhe Institute of Technology (KIT), Karlsruhe, Germany	X-SPEC[133]		70 eV–15 keV; 50–2000 eV for soft XES and RIXS experiments	$E/\Delta E$: 2000–4000 (soft XES and RIXS experiments)
PETRA III, Hamburg, Germany	P01	IRIXS	2.5–90 keV (unique for 2.4–4 keV (Tender X-ray))	1 meV to about 1 eV
Swiss X-ray Free Electron Laser (SwissFEL), Villingen, Switzerland	Athos	Furka	400–1900 eV	200 meV (design RP, $E/\Delta E$ up to 15 000)
Swiss Light Source (SLS), Villingen, Switzerland	3M	ADRESS	300–1600 eV	$E/\Delta E$@1 keV: up to 33000
	10D[134]	SuperXAS	4.5–30 keV (4.5–15 keV for XES and RIXS experiments)	$\Delta E/E$, Si (111): 2.0×10^{-4}; $\Delta E/E$, Si (311): 0.5×10^{-4}; 0.4–2 eV for X-rays between 4.5 keV and 15 keV

(*Continued on next page*)

Table 1. *Continued*

Synchrotron	Beamline/Station	Energy range	Resolution/Resolving power (RP)
Diamond Light Source (DLS), Harwell, UK	I20	Si (111): 4.5–20 keV; Si $(311)^{+}$: 7–34 keV	ΔE/E, Si (111): 1.3×10^{-4}; ΔE/E, Si $(311)^{+}$: 2.8×10^{-5}
	I21	250–3000 eV	E/ΔE: 10000–40000@1000 eV; combined energy resolution at 930 eV: 100 meV (high flux mode), 60 meV (high resolution mode), 35 meV (ultra-high resolution mode)
ELETTRA, Trieste, Italy	BACH	44–1650 eV	0.006 eV@44 eV, 0.35 eV@1650 eV, 0.025 eV@500 eV; E/ΔE: 6.6×10^{3}@870 eV, 1.5×10^{4}@530 eV, 1.2×10^{4}@400 eV, 1.2×10^{4}@90 eV, 1.6×10^{4}@50 eV, 5.5×10^{3}@1650 eV
PAL-XFEL, Pohang, Korea	XAS/XES endstation[135]	270–1200 eV	1500@900 eV (RIXS)
Pohang Light Source (PLS II), Pohang, Korea	1C	2.1–23 keV (DCM Si (111)), 5–23 keV (Mo/B4C multilayer, ∼1%BW); 2.3–16.8 keV for RIXS	∼16 meV (dispersion compensation module, DCM) (RIXS)
NanoTerasu, Hyogo, Japan	BL02U	450–1000 eV	high resolution mode: 40000@532.5 eV, 25000@930 eV; ultrahigh resolution mode: 55000@532.5 eV, 50000@930 eV
Super Photon Ring-8 GeV (SPring8), Hyogo, Japan	BL11XU	6–70 keV; 6–12 keV for RIXS	ΔE/E: $\sim 1 \times 10^{-4}$; ∼1 eV for RIXS
	BL12XU	4.5–30 keV	1.4×10^{-4} (Si (111) bicrystalline spectrometer); 1×10^{-5}–1×10^{-7} (high-resolution monochromator); 0.01–1 eV for RIXS
	BL07LXU[136]	250–2000 eV	E/ΔE: >10000
Taiwan Photon Source (TPS), Hsinchu, Taiwan	41A	400–1200 eV	E/ΔE: 40000–60000 (initial target), 100000 (final goal)
SIRIUS, Ribeirão Preto, Brazil	IPÊ	100–2000 eV; 200–1200 eV for RIXS	60000@930 eV, cff = 5; E/ΔE: ∼8000, target RP > 30000 (with full length undulator, RIXS)
Shanghai Synchrotron Radiation Facility (SSRF), Shanghai, China	BL09U	20–2000 eV (250–1700 eV for RIXS)	maximum 35000@867 eV; 60–90 meV@930 eV for RIXS
Canadian Light Souce (CLS), Saskatoon, Canada	10ID-2 REIXS	95–2000 eV	ΔE/E: 5×10^{-5}@100 eV, 1.3×10^{-4}@1000 eV
Advanced Photon Source (APS), Argonne, USA	27-ID-B	5–14 keV	ΔE/E: 3×10^{-6}; 10–200 meV for RIXS
	30-ID-B,C	23.7–23.9 keV	ΔE/E, cryo-cooled Si (111): 1×10^{-4}; ΔE/E, six-bounce Si HRM (high-resolution monochromator): 4×10^{-8}; ∼1.5 meV for HERIXS

(*Continued on next page*)

Table 1. *Continued*

Synchrotron	Beamline/Station		Energy range	Resolution/Resolving power (RP)
National Synchrotron Light Source (NSLS), Brookhaven, USA	2-ID (SIX)		165–2300 eV	four energy resolution modes: 90/50/30/14 meV@1 keV
Advanced Light Source (ALS), Berkeley, USA	8.0.1	8.0.1.1 (iRIXS) 8.0.1.2 (open port) 8.0.1.3 (qRIXS) 8.0.1.4 (wetRIXS)	80–1250 eV	5000 (slit size dependent)
	6.0.1 (under commissioning)	AMBER	250–2500 eV	calculated RP: 10000@C = 2; 30000@C = 4
	6.0.2 (under development)	QERLIN	290–1500 eV	–
Stanford Synchrotron Radiation Laboratory (SSRL), Stanford, USA	6-2a[137]		2.36–17.5 keV (focused)	ΔE/E, focused: ∼1 × 10^{-4}
	13–2		180–1450 eV (focused)	ΔE/E, focused: 1 × 10^{-4}; 1.5 eV (soft X-ray range)
	15–2[138]		4.8–18.2 keV (focused); 18–24 keV (unfocused)	ΔE/E, focused: 1.0–15, 1 × 10^{-5}; ΔE/E, unfocused: 1 × 10^{-4}

learning could potentially aid in the discovery of new materials with optimal properties for energy conversion and storage applications, as well as the optimization of existing materials and systems. However, the decision to incorporate machine learning will depend on the maturity of RIXS technique and the expertise of the research team.

Furthermore, the broader impact of RIXS on material characterization and *in situ*/operando studies cannot be overlooked. RIXS provides unique insights into the electronic structures and chemical environments of materials, enabling researchers to monitor and understand the dynamic changes that occur during energy conversion and storage processes. This capability is crucial for the development of more efficient and sustainable energy technologies.

In conclusion, the future of RIXS in the fields of energy conversion and storage is promising. By establishing an integrated RIXS database, exploring synergies with other technologies (including potential applications of machine learning), and deepening our understanding of material characterization and *in situ*/operando studies, RIXS will play an increasingly important role in advancing our understanding and development of renewable energy technologies.

ACKNOWLEDGMENTS

We thank the Basic and Applied Basic Research Foundation of Guangdong Province (2022B1515120079), National Natural Science Foundation of China (51803042 and 52272241), International Science and Technology Cooperation Project in Huangpu District (2023GH07), Zhejiang Provincial Natural Science Foundation (No. LR24E020001). G.Z. thanks for the support from the Marcelle-Gauvreau Engineering Research Chair program.

AUTHOR CONTRIBUTIONS

Writing – original draft, R.H. and L.X.; writing – review and editing, M.W., Z.C., N.W., L.M., S.Y., and L.W.; supervision, G.Z. and L.D.

DECLARATION OF INTERESTS

The authors declare no competing interests.

REFERENCES

1. Cano, Z.P., Banham, D., Ye, S., Hintennach, A., Lu, J., Fowler, M., and Chen, Z. (2018). Batteries and fuel cells for emerging electric vehicle markets. Nat. Energy *3*, 279–289. https://doi.org/10.1038/s41560-018-0108-1.
2. Herranz, J., Durst, J., Fabbri, E., Patru, A., Cheng, X., Permyakova, A. A., and Schmidt, T.J. (2016). Interfacial effects on the catalysis of the hydrogen evolution, oxygen evolution and CO_2-reduction reactions for (co-)electrolyzer development. Nano Energy *29*, 4–28. https://doi.org/10.1016/j.nanoen.2016.01.027.
3. Ithisuphalap, K., Zhang, H., Guo, L., Yang, Q., Yang, H., and Wu, G. (2018). Photocatalysis and photoelectrocatalysis methods of nitrogen reduction for sustainable ammonia synthesis. Small Meth *3*, 1800352. https://doi.org/10.1002/smtd.201800352.
4. Du, L., Shao, Y., Sun, J., Yin, G., Du, C., and Wang, Y. (2018). Electrocatalytic valorisation of biomass derived chemicals. Catal. Sci. Technol. *8*, 3216–3232. https://doi.org/10.1039/c8cy00533h.
5. Du, L., Prabhakaran, V., Xie, X., Park, S., Wang, Y., and Shao, Y. (2021). Low-PGM and PGM-free catalysts for proton exchange membrane fuel

cells: stability challenges and material solutions. Adv. Mater. *33*, e1908232. https://doi.org/10.1002/adma.201908232.

6. Liu, X., Xu, G.-L., Kolluru, V.S.C., Zhao, C., Li, Q., Zhou, X., Liu, Y., Yin, L., Zhuo, Z., Daali, A., et al. (2022). Origin and regulation of oxygen redox instability in high-voltage battery cathodes. Nat. Energy *7*, 808–817. https://doi.org/10.1038/s41560-022-01036-3.
7. Pei, Y., Chen, Q., Wang, M., Zhang, P., Ren, Q., Qin, J., Xiao, P., Song, L., Chen, Y., Yin, W., et al. (2022). A medium-entropy transition metal oxide cathode for high-capacity lithium metal batteries. Nat. Commun. *13*, 6158. https://doi.org/10.1038/s41467-022-33927-0.
8. Thomas, O. (2025). Resonant inelastic X-ray scattering in energy materials research and beyond. Nat. Rev. Clean Technol. *1*, 234. https://doi.org/10.1038/s44359-025-00048-y.
9. Xu, R., Du, L., Adekoya, D., Zhang, G., Zhang, S., Sun, S., and Lei, Y. (2020). Well-defined nanostructures for electrochemical energy conversion and storage. Adv. Energy Mater. *11*, 2001537. https://doi.org/10.1002/aenm.202001537.
10. Yang, F., Feng, X., Liu, Y.S., Kao, L.C., Glans, P.A., Yang, W., and Guo, J. (2021). In situ/operando (soft) X-ray spectroscopy study of beyond lithium-ion batteries. Energy Environ. Mater. *4*, 139–157. https://doi.org/10.1002/eem2.12172.
11. Xu, J., Cai, X., Cai, S., Shao, Y., Hu, C., Lu, S., and Ding, S. (2023). High-energy lithium-ion batteries: Recent progress and a promising future in applications. Energy Environ. Mater. *6*, e12450. https://doi.org/10.1002/eem2.12450.
12. Goodenough, J.B., and Park, K.S. (2013). The Li-ion rechargeable battery: A perspective. J. Am. Chem. Soc. *135*, 1167–1176. https://doi.org/10.1021/ja3091438.
13. Li, B., Zhuo, Z., Zhang, L., Iadecola, A., Gao, X., Guo, J., Yang, W., Morozov, A.V., Abakumov, A.M., and Tarascon, J.-M. (2023). Decoupling the roles of Ni and Co in anionic redox activity of Li-rich NMC cathodes. Nat. Mater. *22*, 1370–1379. https://doi.org/10.1038/s41563-023-01679-x.
14. Yang, T., Zhang, K., Zuo, Y., Song, J., Yang, Y., Gao, C., Chen, T., Wang, H., Xiao, W., Jiang, Z., and Xia, D. (2024). Ultrahigh-nickel layered cathode with cycling stability for sustainable lithium-ion batteries. Nat. Sustain. *7*, 1204–1214. https://doi.org/10.1038/s41893-024-01402-x.
15. Zhong, X., Oubla, M., Wang, X., Huang, Y., Zeng, H., Wang, S., Liu, K., Zhou, J., He, L., Zhong, H., et al. (2021). Boosting oxygen reduction activity and enhancing stability through structural transformation of layered lithium manganese oxide. Nat. Commun. *12*, 3136. https://doi.org/10.1038/s41467-021-23430-3.
16. Wang, P., Shao, Q., and Huang, X. (2018). Updating Pt-based electrocatalysts for practical fuel cells. Joule *2*, 2514–2516. https://doi.org/10.1016/j.joule.2018.11.024.
17. Du, L., Xing, L., Zhang, G., Dubois, M., and Sun, S. (2020). Strategies for engineering high-performance PGM-free catalysts toward oxygen reduction and evolution reactions. Small Meth *4*, 2000016. https://doi.org/10.1002/smtd.202000016.
18. Du, L., Xing, L., Zhang, G., and Sun, S. (2020). Metal-organic framework derived carbon materials for electrocatalytic oxygen reactions: Recent progress and future perspectives. Carbon *156*, 77–92. https://doi.org/10.1016/j.carbon.2019.09.029.
19. Li, J., Chen, M., Cullen, D.A., Hwang, S., Wang, M., Li, B., Liu, K., Karakalos, S., Lucero, M., Zhang, H., et al. (2018). Atomically dispersed manganese catalysts for oxygen reduction in proton-exchange membrane fuel cells. Nat. Catal. *1*, 935–945. https://doi.org/10.1038/s41929-018-0164-8.
20. Du, L., Du, C., Chen, G., Kong, F., Yin, G., and Wang, Y. (2016). Metal-organic coordination networks: Prussian blue and its synergy with Pt nanoparticles to enhance oxygen reduction kinetics. ACS Appl. Mater. Interfaces *8*, 15250–15257. https://doi.org/10.1021/acsami.6b02630.
21. Seitz, L.C., Dickens, C.F., Nishio, K., Hikita, Y., Montoya, J., Doyle, A., Kirk, C., Vojvodic, A., Hwang, H.Y., Norskov, J.K., and Jaramillo, T.F. (2016). A highly active and stable $IrO_x/SrIrO_3$ catalyst for the oxygen evolution reaction. Science *353*, 1011–1014. https://doi.org/10.1126/science.aaf5050.
22. Du, L., Luo, L., Feng, Z., Engelhard, M., Xie, X., Han, B., Sun, J., Zhang, J., Yin, G., Wang, C., et al. (2017). Nitrogen-doped graphitized carbon shell encapsulated NiFe nanoparticles: A highly durable oxygen evolution catalyst. Nano Energy *39*, 245–252. https://doi.org/10.1016/j.nanoen.2017.07.006.
23. Han, N., Zhang, W., Guo, W., Pan, H., Jiang, B., Xing, L., Tian, H., Wang, G., Zhang, X., and Fransaer, J. (2023). Designing oxide catalysts for oxygen electrocatalysis: Insights from mechanism to application. Nano-Micro Lett. *15*, 185. https://doi.org/10.1007/s40820-023-01152-z.
24. Kwon, G., Chang, S.H., Heo, J.E., Lee, K.J., Kim, J.-K., Cho, B.-G., Koo, T.Y., Kim, B.J., Kim, C., Lee, J.H., et al. (2021). Experimental verification of Ir 5d orbital states and atomic structures in highly active amorphous iridium oxide catalysts. ACS Catal. *11*, 10084–10094. https://doi.org/10.1021/acscatal.1c00818.
25. Di, J., Xiong, J., Li, H., and Liu, Z. (2018). Ultrathin 2D photocatalysts: Electronic-structure tailoring, hybridization, and applications. Adv. Mater. *30*, 1704548. https://doi.org/10.1002/adma.201704548.
26. Liu, G., Xun, S., Vukmirovic, N., Song, X., Olalde-Velasco, P., Zheng, H., Battaglia, V.S., Wang, L., and Yang, W. (2011). Polymers with tailored electronic structure for high capacity lithium battery electrodes. Adv. Mater. *23*, 4679–4683. https://doi.org/10.1002/adma.201102421.
27. Du, L., Zhang, S., Chen, G., Yin, G., Du, C., Tan, Q., Sun, Y., Qu, Y., and Gao, Y. (2014). Polyelectrolyte assisted synthesis and enhanced oxygen reduction activity of Pt nanocrystals with controllable shape and size. ACS Appl. Mater. Interfaces *6*, 14043–14049. https://doi.org/10.1021/am503372f.
28. Dean, D.P., Deshmukh, G.S., Russell, C.K., Zhu, K., Li, C.W., Greeley, J. P., Leshchev, D., Stavitski, E., and Miller, J.T. (2024). Valence-to-core X-ray emission spectroscopy to resolve the size-dependent valence electronic structure of Pt nanoparticles. Catal. Sci. Technol. *14*, 2580–2592. https://doi.org/10.1039/d3cy01554h.
29. Cheng, C., Zhuo, Z., Chen, S., Zhou, X., Yuan, C., Zeng, P., Guo, J., and Zhang, L. (2024). Cationic and anionic redox of battery cathodes investigated by advanced synchrotron-based mapping of resonant inelastic X-ray scattering. Adv. Funct. Mater. *34*, 2403442. https://doi.org/10.1002/adfm.202403442.
30. Wu, J., Zhuo, Z., Rong, X., Dai, K., Lebens-Higgins, Z., Sallis, S., Pan, F., Piper, L.F.J., Liu, G., Chuang, Y.D., et al. (2020). Dissociate lattice oxygen redox reactions from capacity and voltage drops of battery electrodes. Sci. Adv. *6*, eaaw3871. https://doi.org/10.1126/sciadv.aaw3871.
31. Gent, W.E., Lim, K., Liang, Y., Li, Q., Barnes, T., Ahn, S.J., Stone, K.H., McIntire, M., Hong, J., Song, J.H., et al. (2017). Coupling between oxygen redox and cation migration explains unusual electrochemistry in lithium-rich layered oxides. Nat. Commun. *8*, 2091. https://doi.org/10.1038/s41467-017-02041-x.
32. House, R.A., Marie, J.-J., Pérez-Osorio, M.A., Rees, G.J., Boivin, E., and Bruce, P.G. (2021). The role of O_2 in O-redox cathodes for Li-ion batteries. Nat. Energy *6*, 781–789. https://doi.org/10.1038/s41560-021-00780-2.
33. Gao, X., Li, B., Kummer, K., Geondzhian, A., Aksyonov, D.A., Dedryvère, R., Foix, D., Rousse, G., Ben Yahia, M., Doublet, M.-L., et al. (2025). Clarifying the origin of molecular O_2 in cathode oxides. Nat. Mater. *24*, 743–752. https://doi.org/10.1038/s41563-025-02144-7.
34. Marie, J.-J., House, R.A., Rees, G.J., Robertson, A.W., Jenkins, M., Chen, J., Agrestini, S., Garcia-Fernandez, M., Zhou, K.-J., and Bruce, P.G. (2024). Trapped O_2 and the origin of voltage fade in layered Li-rich cathodes. Nat. Mater. *23*, 818–825. https://doi.org/10.1038/s41563-024-01833-z.
35. Yang, L., Shui, J., Du, L., Shao, Y., Liu, J., Dai, L., and Hu, Z. (2019). Carbon-based metal-free ORR electrocatalysts for fuel cells: Past, present,

and future. Adv. Mater. *31*, e1804799. https://doi.org/10.1002/adma.201804799.

36. Wan, L., Zhou, Q., Wang, X., Wood, T.E., Wang, L., Duchesne, P.N., Guo, J., Yan, X., Xia, M., Li, Y.F., et al. (2019). Cu_2O nanocubes with mixed oxidation-state facets for (photo)catalytic hydrogenation of carbon dioxide. Nat. Catal. *2*, 889–898. https://doi.org/10.1038/s41929-019-0338-z.
37. Shen, H., Gracia-Espino, E., Ma, J., Tang, H., Mamat, X., Wagberg, T., Hu, G., and Guo, S. (2017). Atomically FeN_2 moieties dispersed on mesoporous carbon: A new atomic catalyst for efficient oxygen reduction catalysis. Nano Energy *35*, 9–16. https://doi.org/10.1016/j.nanoen.2017.03.027.
38. Huang, J., Lu, Q., Ma, X., and Yang, X. (2018). Bio-inspired FeN_5 moieties anchored on a three-dimensional graphene aerogel to improve oxygen reduction catalytic performance. J. Mater. Chem. A *6*, 18488–18497. https://doi.org/10.1039/c8ta06455e.
39. Zhu, Y., Zhang, B., Liu, X., Wang, D.W., and Su, D.S. (2014). Unravelling the structure of electrocatalytically active Fe-N complexes in carbon for the oxygen reduction reaction. Angew. Chem. Int. Ed. *53*, 10673–10677. https://doi.org/10.1002/anie.201405314.
40. Trogadas, P., Parrondo, J., and Ramani, V. (2012). CeO_2 surface oxygen vacancy concentration governs in situ free radical scavenging efficacy in polymer electrolytes. ACS Appl. Mater. Interfaces *4*, 5098–5102. https://doi.org/10.1021/am3016069.
41. Ji, D., Fan, L., Tao, L., Sun, Y., Li, M., Yang, G., Tran, T.Q., Ramakrishna, S., and Guo, S. (2019). The Kirkendall effect for engineering oxygen vacancy of hollow Co_3O_4 nanoparticles toward high-performance portable zinc-air batteries. Angew. Chem. Int. Ed. *58*, 13840–13844. https://doi.org/10.1002/anie.201908736.
42. Qian, Z., Sun, B., Li, X., Du, L., Wang, Y., Du, C., Zuo, P., Ma, Y., and Yin, G. (2020). In-situ formed free-standing Ir nanocatalysts as carbon- and binder-free cathode for rechargeable nonaqueous Li-O_2 batteries. J. Alloys Compd. *832*, 155009. https://doi.org/10.1016/j.jallcom.2020.155009.
43. Sun, W., Du, L., Du, C., Gao, Y., and Yin, G. (2019). Three-dimensional layered double hydroxides on carbon nanofibers: The engineered mass transfer channels and active sites towards oxygen evolution reaction. Appl. Surf. Sci. *485*, 41–47. https://doi.org/10.1016/j.apsusc.2019.03.335.
44. Han, Y., Fang, C., Ji, X., Wei, J., Ge, Q., and Sun, J. (2020). Interfacing with carbonaceous potassium promoters boosts catalytic CO_2 hydrogenation of iron. ACS Catal. *10*, 12098–12108. https://doi.org/10.1021/acscatal.0c03215.
45. Sun, J., Du, L., Sun, B., Han, G., Ma, Y., Wang, J., Huo, H., Zuo, P., Du, C., and Yin, G. (2021). A bifunctional perovskite oxide catalyst: The triggered oxygen reduction/evolution electrocatalysis by moderated Mn-Ni co-doping. J. Energy Chem. *54*, 217–224. https://doi.org/10.1016/j.jechem.2020.05.064.
46. Sun, W., Du, L., Tan, Q., Zhou, J., Hu, Y., Du, C., Gao, Y., and Yin, G. (2019). Engineering of nitrogen coordinated single cobalt atom moieties for oxygen electroreduction. ACS Appl. Mater. Interfaces *11*, 41258–41266. https://doi.org/10.1021/acsami.9b11830.
47. Wang, D., Xiao, L., Yang, P., Xu, Z., Lu, X., Du, L., Levin, O., Ge, L., Pan, X., Zhang, J., and An, M. (2019). Dual-nitrogen-source engineered Fe-Nx moieties as a booster to oxygen electroreduction. J. Mater. Chem. A *7*, 11007–11015. https://doi.org/10.1039/C9TA01953G.
48. Al Samarai, M., Delgado-Jaime, M.U., Ishii, H., Hiraoka, N., Tsuei, K.-D., Rueff, J., Lassale-Kaiser, B., Weckhuysen, B.M., and de Groot, F.M.F. (2016). 1s3p resonant inelastic X-ray scattering of cobalt oxides and sulfides. J. Phys. Chem. C *120*, 24063–24069. https://doi.org/10.1021/acs.jpcc.6b06444.
49. Glatzel, P., Bergmann, U., Yano, J., Visser, H., Robblee, J.H., Gu, W., de Groot, F.M.F., Christou, G., Pecoraro, V.L., Cramer, S.P., and Yachandra, V.K. (2004). The electronic structure of Mn in oxides, coordination complexes, and the oxygen-evolving complex of photosystem II studied by resonant inelastic X-ray scattering. J. Am. Chem. Soc. *126*, 9946–9959. https://doi.org/10.1021/ja038579z.
50. Singh, J., Lamberti, C., and van Bokhoven, J.A. (2010). Advanced X-ray absorption and emission spectroscopy: In situ catalytic studies. Chem. Soc. Rev. *39*, 4754–4766. https://doi.org/10.1039/c0cs00054j.
51. Yan, J.J., Kroll, T., Baker, M.L., Wilson, S.A., Decréau, R., Lundberg, M., Sokaras, D., Glatzel, P., Hedman, B., Hodgson, K.O., and Solomon, E.I. (2019). Resonant inelastic X-ray scattering determination of the electronic structure of oxyhemoglobin and its model complex. Proc. Natl. Acad. Sci. USA *116*, 2854–2859. https://doi.org/10.1073/pnas.1815981116.
52. Yang, W., and Devereaux, T.P. (2018). Anionic and cationic redox and interfaces in batteries: Advances from soft X-ray absorption spectroscopy to resonant inelastic scattering. J. Power Sources *389*, 188–197. https://doi.org/10.1016/j.jpowsour.2018.04.018.
53. Zhuo, Z., Liu, Y.S., Guo, J., Chuang, Y.D., Pan, F., and Yang, W. (2020). Full energy range resonant inelastic X-ray scattering of O_2 and CO_2: Direct comparison with oxygen redox state in batteries. J. Phys. Chem. Lett. *11*, 2618–2623. https://doi.org/10.1021/acs.jpclett.0c00423.
54. Pan, B.Y., Jang, H., Lee, J.S., Sutarto, R., He, F., Zeng, J.F., Liu, Y., Zhang, X.W., Feng, Y., Hao, Y.Q., et al. (2019). Intertwined spin and orbital density waves in MnP uncovered by resonant soft X-ray scattering. Phys. Rev. X *9*, 021055. https://doi.org/10.1103/PhysRevX.9.021055.
55. Takubo, K., Yamamoto, K., Hirata, Y., Wadati, H., Mizokawa, T., Sutarto, R., He, F., Ishii, K., Yamasaki, Y., Nakao, H., et al. (2018). Commensurate versus incommensurate charge ordering near the superconducting dome in $Ir_{1-x}Pt_xTe_2$ revealed by resonant x-ray scattering. Phys. Rev. B *97*, 205142. https://doi.org/10.1103/PhysRevB.97.205142.
56. Qamar, A., Amin, M.R., Grynko, O., Semeniuk, O., Reznik, A., and Moewes, A. (2019). A probe of valence and conduction band electronic structure of lead oxide films for photodetectors. ChemPhysChem *20*, 3328–3335. https://doi.org/10.1002/cphc.201900726.
57. Wu, J., Yang, Y., and Yang, W. (2020). Advances in soft X-ray RIXS for studying redox reaction states in batteries. Dalton T *49*, 13519–13527. https://doi.org/10.1039/d0dt01782e.
58. Gudat, W., and Kunz, C. (1972). Close similarity between photoelectric yield and photoabsorption spectra in the soft-X-ray range. Phys. Rev. Lett. *29*, 169–172. https://doi.org/10.1103/PhysRevLett.29.169.
59. Cesar, A., Gel'mukhanov, F., Luo, Y., Ågren, H., Skytt, P., Glans, P., Guo, J., Gunnelin, K., and Nordgren, J. (1997). Resonant x-ray scattering beyond the Born–Oppenheimer approximation: Symmetry breaking in the oxygen resonant x-ray emission spectrum of carbon dioxide. J. Chem. Phys. *106*, 3439–3456. https://doi.org/10.1063/1.474111.
60. Glatzel, P., Singh, J., Kvashnina, K.O., and van Bokhoven, J.A. (2010). In situ characterization of the 5d density of states of Pt nanoparticles upon adsorption of CO. J. Am. Chem. Soc. *132*, 2555–2557. https://doi.org/10.1021/ja907760p.
61. Duda, L.C., and Edström, K. (2017). Oxygen redox reactions in Li ion battery electrodes studied by resonant inelastic X-ray scattering. J. Electron. Spectrosc. Relat. Phenom. *221*, 79–87. https://doi.org/10.1016/j.elspec.2017.06.003.
62. Li, Q., Yan, S., and Yang, W. (2020). Interfacial properties in energy storage systems studied by soft x-ray absorption spectroscopy and resonant inelastic x-ray scattering. J. Chem. Phys. *152*, 140901. https://doi.org/10.1063/5.0003311.
63. Achkar, A.J., Regier, T.Z., Wadati, H., Kim, Y.J., Zhang, H., and Hawthorn, D.G. (2011). Bulk sensitive x-ray absorption spectroscopy free of self-absorption effects. Phys. Rev. B *83*, 081106. https://doi.org/10.1103/PhysRevB.83.081106.
64. Kotani, A., and Shin, S. (2001). Resonant inelastic x-ray scattering spectra for electrons in solids. Rev. Mod. Phys. *73*, 203–246. https://doi.org/10.1103/RevModPhys.73.203.

65. Kotani, A. (2005). Resonant inelastic X-ray scattering in d and f electron systems. Eur. Phys. J. B *47*, 3–27. https://doi.org/10.1140/epjb/e2005-00303-4.

66. Brink, J.v.d., Pavarini, E., Koch, E., Brink, J.v.d., and Sawatzky, G. (2016). Resonant Inelastic X-ray Scattering on Elementary Excitations. In Quantum Materials: Experiments and Theory Modeling and Simulation (Forschungszentrum Jülich GmbH), pp. 2–11.

67. Ament, L.J.P., van Veenendaal, M., Devereaux, T.P., Hill, J.P., and van den Brink, J. (2011). Resonant inelastic x-ray scattering studies of elementary excitations. Rev. Mod. Phys. *83*, 705–767. https://doi.org/10.1103/RevModPhys.83.705.

68. Horrocks, G.A., De Jesus, L.R., Andrews, J.L., and Banerjee, S. (2017). X-ray spectroscopy and imaging as multiscale probes of intercalation phenomena in cathode materials. Jom *69*, 1469–1477. https://doi.org/10.1007/s11837-017-2398-3.

69. van Schooneveld, M.M., Kurian, R., Juhin, A., Zhou, K., Schlappa, J., Strocov, V.N., Schmitt, T., and de Groot, F.M.F. (2012). Electronic structure of CoO nanocrystals and a single crystal probed by resonant X-ray emission spectroscopy. J. Phys. Chem. C *116*, 15218–15230. https://doi.org/10.1021/jp302847h.

70. Jeyachandran, Y.L., Meyer, F., Nagarajan, S., Benkert, A., Bär, M., Blum, M., Yang, W., Reinert, F., Heske, C., Weinhardt, L., and Zharnikov, M. (2014). Ion-solvation-induced molecular reorganization in liquid water probed by resonant inelastic soft X-ray scattering. J. Phys. Chem. Lett. *5*, 4143–4148. https://doi.org/10.1021/jz502186a.

71. Xue, Z., Li, J., Pianetta, P., and Liu, Y. (2022). Data-driven lithium-ion battery cathode research with state-of-the-art synchrotron X-ray techniques. Acc. Mater. Res. *3*, 854–865. https://doi.org/10.1021/accountsmr.2c00098.

72. Pastor, E., Sachs, M., Selim, S., Durrant, J.R., Bakulin, A.A., and Walsh, A. (2022). Electronic defects in metal oxide photocatalysts. Nat. Rev. Mater. *7*, 503–521. https://doi.org/10.1038/s41578-022-00433-0.

73. House, R.A., Rees, G.J., McColl, K., Marie, J.-J., Garcia-Fernandez, M., Nag, A., Zhou, K.-J., Cassidy, S., Morgan, B.J., Saiful Islam, M., and Bruce, P.G. (2023). Delocalized electron holes on oxygen in a battery cathode. Nat. Energy *8*, 351–360. https://doi.org/10.1038/s41560-023-01211-0.

74. Aktekin, B., Massel, F., Ahmadi, M., Valvo, M., Hahlin, M., Zipprich, W., Marzano, F., Duda, L., Younesi, R., Edström, K., and Brandell, D. (2020). How Mn/Ni ordering controls electrochemical performance in high-voltage spinel $LiNi_{0.4}4Mn_{1.56}O_4$ with fixed oxygen content. ACS Appl. Energy Mater. *3*, 6001–6013. https://doi.org/10.1021/acsaem.0c01075.

75. Wegener, E.C., Bukowski, B.C., Yang, D., Wu, Z., Kropf, A.J., Delgass, W.N., Greeley, J., Zhang, G., and Miller, J.T. (2020). Intermetallic compounds as an alternative to single-atom alloy catalysts: Geometric and electronic structures from advanced X-ray spectroscopies and computational studies. ChemCatChem *12*, 1325–1333. https://doi.org/10.1002/cctc.201901869.

76. Wu, H., Wang, Y., Shi, Z., Wang, X., Yang, J., Xiao, M., Ge, J., Xing, W., and Liu, C. (2022). Recent developments of iridium-based catalysts for the oxygen evolution reaction in acidic water electrolysis. J. Mater. Chem. A *10*, 13170–13189. https://doi.org/10.1039/d1ta10324e.

77. Wu, J., Li, Q., Sallis, S., Zhuo, Z., Gent, W.E., Chueh, W.C., Yan, S., Chuang, Y.-d., and Yang, W. (2019). Fingerprint oxygen redox reactions in batteries through high-efficiency mapping of resonant inelastic X-ray scattering. Condensed Matter *4*, 5. https://doi.org/10.3390/condmat4010005.

78. Tesch, M.F., Bonke, S.A., Jones, T.E., Shaker, M.N., Xiao, J., Skorupska, K., Mom, R., Melder, J., Kurz, P., Knop-Gericke, A., et al. (2019). Evolution of oxygen-metal electron transfer and metal electronic states during manganese oxide catalyzed water oxidation revealed with in situ soft X-ray spectroscopy. Angew. Chem. Int. Ed. *58*, 3426–3432. https://doi.org/10.1002/anie.201810825.

79. Zhang, J.-N., Li, Q., Ouyang, C., Yu, X., Ge, M., Huang, X., Hu, E., Ma, C., Li, S., Xiao, R., et al. (2019). Trace doping of multiple elements enables stable battery cycling of $LiCoO_2$ at 4.6 V. Nat. Energy *4*, 594–603. https://doi.org/10.1038/s41560-019-0409-z.

80. Wu, J., Zhang, X., Zheng, S., Liu, H., Wu, J., Fu, R., Li, Y., Xiang, Y., Liu, R., Zuo, W., et al. (2020). Tuning oxygen redox reaction through the inductive effect with proton insertion in Li-rich oxides. ACS Appl. Mater. Interfaces *12*, 7277–7284. https://doi.org/10.1021/acsami.9b21738.

81. Zhu, X., Meng, F., Zhang, Q., Xue, L., Zhu, H., Lan, S., Liu, Q., Zhao, J., Zhuang, Y., Guo, Q., et al. (2020). $LiMnO_2$ cathode stabilized by interfacial orbital ordering for sustainable lithium-ion batteries. Nat. Sustain. *4*, 392–401. https://doi.org/10.1038/s41893-020-00660-9.

82. Li, N., Sallis, S., Papp, J.K., McCloskey, B.D., Yang, W., and Tong, W. (2020). Correlating the phase evolution and anionic redox in Co-Free Ni-Rich layered oxide cathodes. Nano Energy *78*, 105365. https://doi.org/10.1016/j.nanoen.2020.105365.

83. Boivin, E., House, R.A., Pérez-Osorio, M.A., Marie, J.-J., Maitra, U., Rees, G.J., and Bruce, P.G. (2021). Bulk O_2 formation and Mg displacement explain O-redox in $Na_{0.67}Mn_{0.72}Mg_{0.28}O_2$. Joule *5*, 1267–1280. https://doi.org/10.1016/j.joule.2021.04.006.

84. Hu, E., Li, Q., Wang, X., Meng, F., Liu, J., Zhang, J.-N., Page, K., Xu, W., Gu, L., Xiao, R., et al. (2021). Oxygen-redox reactions in $LiCoO_2$ cathode without O-O bonding during charge-discharge. Joule *5*, 720–736. https://doi.org/10.1016/j.joule.2021.01.006.

85. Wang, J., Kim, S.-J., Liu, J., Gao, Y., Choi, S., Han, J., Shin, H., Jo, S., Kim, J., Ciucci, F., et al. (2021). Redirecting dynamic surface restructuring of a layered transition metal oxide catalyst for superior water oxidation. Nat. Catal. *4*, 212–222. https://doi.org/10.1038/s41929-021-00578-1.

86. Hirsbrunner, M., Mikheenkova, A., Törnblom, P., House, R.A., Zhang, W., Asmara, T.C., Wei, Y., Schmitt, T., Rensmo, H., Mukherjee, S., et al. (2024). Vibrationally-resolved RIXS reveals OH-group formation in oxygen redox active Li-ion battery cathodes. Phys. Chem. Chem. Phys. *26*, 19460–19468. https://doi.org/10.1039/d4cp01766h.

87. Wang, J., Hsu, C.-S., Wu, T.-S., Chan, T.-S., Suen, N.-T., Lee, J.-F., and Chen, H.M. (2023). In situ X-ray spectroscopies beyond conventional X-ray absorption spectroscopy on deciphering dynamic configuration of electrocatalysts. Nat. Commun. *14*, 6576. https://doi.org/10.1038/s41467-023-42370-8.

88. Liu, H., Hua, W., Kunz, S., Bianchini, M., Li, H., Peng, J., Lin, J., Dolotko, O., Bergfeldt, T., Wang, K., et al. (2024). Tailoring superstructure units for improved oxygen redox activity in Li-rich layered oxide battery's positive electrodes. Nat. Commun. *15*, 9981. https://doi.org/10.1038/s41467-024-54312-z.

89. Wang, X., Zhang, Q., Zhao, C., Li, H., Zhang, B., Zeng, G., Tang, Y., Huang, Z., Hwang, I., Zhang, H., et al. (2024). Achieving a high-performance sodium-ion pouch cell by regulating intergrowth structures in a layered oxide cathode with anionic redox. Nat. Energy *9*, 184–196. https://doi.org/10.1038/s41560-023-01425-2.

90. Traulsen, M.L., de Carvalho, H.W.P., Zielke, P., and Grunwaldt, J.D. (2017). The effect of electrical polarization on electronic structure in LSM electrodes: An operando XAS, RIXS and XES study. J. Electrochem. Soc. *164*, F3064–F3072. https://doi.org/10.1149/2.0091710jes.

91. Al Samarai, M., Hahn, A.W., Beheshti Askari, A., Cui, Y.T., Yamazoe, K., Miyawaki, J., Harada, Y., Rüdiger, O., and DeBeer, S. (2019). Elucidation of structure-activity correlations in a nickel manganese oxide oxygen evolution reaction catalyst by operando Ni L-edge X-ray absorption spectroscopy and 2p3d resonant inelastic X-ray scattering. ACS Appl. Mater. Interfaces *11*, 38595–38605. https://doi.org/10.1021/acsami.9b06752.

92. Hadt, R.G., Hayes, D., Brodsky, C.N., Ullman, A.M., Casa, D.M., Upton, M.H., Nocera, D.G., and Chen, L.X. (2016). X-ray spectroscopic characterization of Co(IV) and metal-metal interactions in Co_4O_4: Electronic

structure contributions to the formation of high-valent states relevant to the oxygen evolution reaction. J. Am. Chem. Soc. *138*, 11017–11030. https://doi.org/10.1021/jacs.6b04663.

93. Hennies, F., Pietzsch, A., Berglund, M., Föhlisch, A., Schmitt, T., Strocov, V., Karlsson, H.O., Andersson, J., and Rubensson, J.-E. (2010). Resonant inelastic scattering spectra of free molecules with vibrational resolution. Phys. Rev. Lett. *104*, 193002. https://doi.org/10.1103/PhysRevLett.104.193002.

94. Weinhardt, L., Blum, M., Fuchs, O., Benkert, A., Meyer, F., Bär, M., Denlinger, J.D., Yang, W., Reinert, F., and Heske, C. (2013). RIXS investigations of liquids, solutions, and liquid/solid interfaces. J. Electron Spectrosc *188*, 111–120. https://doi.org/10.1016/j.elspec.2012.10.006.

95. Huang, J., Zhong, P., Ha, Y., Kwon, D.-H., Crafton, M.J., Tian, Y., Balasubramanian, M., McCloskey, B.D., Yang, W., and Ceder, G. (2021). Non-topotactic reactions enable high rate capability in Li-rich cathode materials. Nat. Energy *6*, 706–714. https://doi.org/10.1038/s41560-021-00817-6.

96. Zhou, B., Wong, D., Fu, Z., Guo, H., Schulz, C., Karkera, G., Hahn, H., Bianchini, M., and Wang, Q. (2024). K-doping suppresses oxygen redox in P2-$Na_{0.67}Ni_{0.11}Cu_{0.22}Mn_{0.67}O_2$ cathode materials for sodium-ion batteries. Small *20*, 2402991. https://doi.org/10.1002/smll.202402991.

97. Lyu, Y., Wu, X., Wang, K., Feng, Z., Cheng, T., Liu, Y., Wang, M., Chen, R., Xu, L., Zhou, J., et al. (2020). An overview on the advances of $LiCoO_2$ cathodes for lithium-ion batteries. Adv. Energy Mater. *11*, 2000982. https://doi.org/10.1002/aenm.202000982.

98. Li, L., Castro, F.C., Park, J.S., Li, H., Lee, E., Boyko, T.D., Freeland, J.W., Yao, Z., Fister, T.T., Vinson, J., et al. (2019). Probing electrochemically induced structural evolution and oxygen redox reactions in layered lithium iridate. Chem. Mater. *31*, 4341–4352. https://doi.org/10.1021/acs.chemmater.8b04591.

99. Li, N., Sallis, S., Papp, J.K., Wei, J., McCloskey, B.D., Yang, W., and Tong, W. (2019). Unraveling the cationic and anionic redox reactions in a conventional layered oxide cathode. ACS Energy Lett. *4*, 2836–2842. https://doi.org/10.1021/acsenergylett.9b02147.

100. Luo, K., Roberts, M.R., Hao, R., Guerrini, N., Pickup, D.M., Liu, Y.S., Edström, K., Guo, J., Chadwick, A.V., Duda, L.C., and Bruce, P.G. (2016). Charge-compensation in 3d-transition-metal-oxide intercalation cathodes through the generation of localized electron holes on oxygen. Nat. Chem. *8*, 684–691. https://doi.org/10.1038/nchem.2471.

101. Zhang, J., Wang, Q., Li, S., Jiang, Z., Tan, S., Wang, X., Zhang, K., Yuan, Q., Lee, S.-J., Titus, C.J., et al. (2020). Depth-dependent valence stratification driven by oxygen redox in lithium-rich layered oxide. Nat. Commun. *11*, 6342. https://doi.org/10.1038/s41467-020-20198-w.

102. House, R.A., Marie, J.-J., Park, J., Rees, G.J., Agrestini, S., Nag, A., Garcia-Fernandez, M., Zhou, K.-J., and Bruce, P.G. (2021). Covalency does not suppress O_2 formation in 4d and 5d Li-rich O-redox cathodes. Nat. Commun. *12*, 2975. https://doi.org/10.1038/s41467-021-23154-4.

103. Marie, J.J., Jenkins, M., Chen, J., Rees, G., Cellorio, V., Choi, J., Agrestini, S., Garcia-Fernandez, M., Zhou, K.J., House, R.A., and Bruce, P.G. (2024). Reversible electron-holes on O in P2-type $Na_{0.67}Li_{0.1}Ni_{0.3}Mn_{0.6}O_2$. Adv. Energy Mater. *14*, 2401935. https://doi.org/10.1002/aenm.202401935.

104. Jacquet, Q., Mozhzhukhina, N., Gillespie, P.N.O., Wittmann, G., Ramirez, L.P., Capone, F.G., Rueff, J.P., Belin, S., Dedryvère, R., Stievano, L., et al. (2024). A fundamental correlative spectroscopic study on $Li_{1-x}NiO_2$ and $NaNiO_2$. Adv. Energy Mater. *14*, 2401413. https://doi.org/10.1002/aenm.202401413.

105. Wang, Q., Zhou, D., Zhao, C., Wang, J., Guo, H., Wang, L., Yao, Z., Wong, D., Schuck, G., Bai, X., et al. (2024). Fast-charge high-voltage layered cathodes for sodium-ion batteries. Nat. Sustain. *7*, 338–347. https://doi.org/10.1038/s41893-024-01266-1.

106. Reuss, T., Nair Lalithambika, S.S., David, C., Döring, F., Jooss, C., Risch, M., and Techert, S. (2023). Advancements in liquid jet technology and X-ray spectroscopy for understanding energy conversion materials during operation. Acc. Chem. Res. *56*, 203–214. https://doi.org/10.1021/acs.accounts.2c00525.

107. Hallmann, J., Grübel, S., Rajkovic, I., Quevedo, W., Busse, G., Scholz, M., More, R., Petri, M., and Techert, S. (2010). First steps towards probing chemical systems and dynamics with free-electron laser radiation-case studies at the FLASH facility. J. Phys. B: At. Mol. Opt. Phys. *43*, 194009. https://doi.org/10.1088/0953-4075/43/19/194009.

108. Busse, P., Yin, Z., Mierwaldt, D., Scholz, J., Kressdorf, B., Glaser, L., Miedema, P.S., Rothkirch, A., Viefhaus, J., Jooss, C., et al. (2020). Probing the surface of $La_{0.6}Sr_{0.4}MnO_3$ in water vapor by in situ photon-in/photon-out spectroscopy. J. Phys. Chem. C *124*, 7893–7902. https://doi.org/10.1021/acs.jpcc.0c00840.

109. Tsuchimoto, A., Shi, X.-M., Kawai, K., Mortemard de Boisse, B., Kikkawa, J., Asakura, D., Okubo, M., and Yamada, A. (2021). Nonpolarizing oxygen-redox capacity without O-O dimerization in $Na_2Mn_3O_7$. Nat. Commun. *12*, 631. https://doi.org/10.1038/s41467-020-20643-w.

110. Dai, K., Wu, J., Zhuo, Z., Li, Q., Sallis, S., Mao, J., Ai, G., Sun, C., Li, Z., Gent, W.E., et al. (2019). High reversibility of lattice oxygen redox quantified by direct bulk probes of both anionic and cationic redox reactions. Joule *3*, 518–541. https://doi.org/10.1016/j.joule.2018.11.014.

111. Zhang, L., Wei, Q., Sun, D., Li, N., Ju, H., Feng, J., Zhu, J., Mai, L., Cairns, E.J., and Guo, J. (2018). Conversion reaction of vanadium sulfide electrode in the lithium-ion cell: Reversible or not reversible? Nano Energy *51*, 391–399. https://doi.org/10.1016/j.nanoen.2018.06.076.

112. Kavčič, M., Bučar, K., Petric, M., Žitnik, M., Arčon, I., Dominko, R., and Vizintin, A. (2016). Operando resonant inelastic X-ray scattering: An appropriate tool to characterize sulfur in Li-S batteries. J. Phys. Chem. C *120*, 24568–24576. https://doi.org/10.1021/acs.jpcc.6b06705.

113. Van Kuiken, B.E., Hahn, A.W., Maganas, D., and DeBeer, S. (2016). Measuring spin-allowed and spin-forbidden d-d excitations in vanadium complexes with 2p3d resonant inelastic X-ray scattering. Inorg. Chem. *55*, 11497–11501. https://doi.org/10.1021/acs.inorgchem.6b02053.

114. Zhang, X., Chen, K., Sun, Z., Hu, G., Xiao, R., Cheng, H.-M., and Li, F. (2020). Structure-related electrochemical performance of organosulfur compounds for lithium-sulfur batteries. Energy Environ. Sci. *13*, 1076–1095. https://doi.org/10.1039/c9ee03848e.

115. Liu, Y.-S., Feng, X., Glans, P.-A., and Guo, J. (2020). In-situ/operando soft X-ray spectroscopy characterization of energy and catalytic materials. Sol. Energy Mater. Sol. Cells *208*, 110432. https://doi.org/10.1016/j.solmat.2020.110432.

116. Amin, M.R., Strobel, P., Qamar, A., Giftthaler, T., Schnick, W., and Moewes, A. (2020). Understanding of luminescence properties using direct measurements on Eu^{2+}-doped wide bandgap phosphors. Adv. Opt. Mater. *8*, 2000504. https://doi.org/10.1002/adom.202000504.

117. Ketabi, N., de Boer, T., Karakaya, M., Zhu, J., Podila, R., Rao, A.M., Kurmaev, E.Z., and Moewes, A. (2016). Tuning the electronic structure of graphene through nitrogen doping: Experiment and theory. RSC Adv. *6*, 56721–56727. https://doi.org/10.1039/c6ra07546k.

118. Ray, K.G., Klebanoff, L.E., Lee, J.R.I., Stavila, V., Heo, T.W., Shea, P., Baker, A.A., Kang, S., Bagge-Hansen, M., Liu, Y.S., et al. (2017). Elucidating the mechanism of MgB_2 initial hydrogenation via a combined experimental-theoretical study. Phys. Chem. Chem. Phys. *19*, 22646–22658. https://doi.org/10.1039/c7cp03709k.

119. McLeod, J.A., Zhao, J., Yang, L., Liu, Y., and Liu, L. (2017). Structural evolution of reduced GeO_x nanoparticles. Phys. Chem. Chem. Phys. *19*, 3182–3191. https://doi.org/10.1039/c6cp07354a.

120. Zhang, Z., Schwanz, D., Narayanan, B., Kotiuga, M., Dura, J.A., Cherukara, M., Zhou, H., Freeland, J.W., Li, J., Sutarto, R., et al. (2018). Perovskite nickelates as electric-field sensors in salt water. Nature *553*, 68–72. https://doi.org/10.1038/nature25008.

121. Jin, L., Liu, B., Wang, P., Yao, H., Achola, L.A., Kerns, P., Lopes, A., Yang, Y., Ho, J., Moewes, A., et al. (2018). Ultrasmall Au nanocatalysts supported on nitrided carbon for electrocatalytic CO_2 reduction: The role

of the carbon support in high selectivity. Nanoscale *10*, 14678–14686. https://doi.org/10.1039/c8nr04322a.

122. Xu, W., Liu, L., Yang, L., Shen, P., Sun, B., and McLeod, J.A. (2016). Dissociation of methylammonium cations in hybrid organic-inorganic perovskite solar cells. Nano Lett. *16*, 4720–4725. https://doi.org/10.1021/acs.nanolett.6b02307.
123. Turner, S., Yan, W., Long, H., Nelson, A.J., Baker, A., Lee, J.R.I., Carraro, C., Worsley, M.A., Maboudian, R., and Zettl, A. (2018). Boron doping and defect engineering of graphene aerogels for ultrasensitive NO_2 detection. J. Phys. Chem. C *122*, 20358–20365. https://doi.org/10.1021/acs.jpcc.8b05984.
124. Andrews, J.L., Mukherjee, A., Yoo, H.D., Parija, A., Marley, P.M., Fakra, S., Prendergast, D., Cabana, J., Klie, R.F., and Banerjee, S. (2018). Reversible Mg-ion insertion in a metastable one-dimensional polymorph of V_2O_5. Chem *4*, 564–585. https://doi.org/10.1016/j.chempr.2017.12.018.
125. Zabolotnyy, V.B., Fürsich, K., Green, R.J., Lutz, P., Treiber, K., Min, C.-H., Dukhnenko, A.V., Shitsevalova, N.Y., Filipov, V.B., Kang, B.Y., et al. (2018). Chemical and valence reconstruction at the surface of SmB_6 revealed by means of resonant soft x-ray reflectometry. Phys. Rev. B *97*, 205416. https://doi.org/10.1103/PhysRevB.97.205416.
126. Chen, Y.Z., Trier, F., Wijnands, T., Green, R.J., Gauquelin, N., Egoavil, R., Christensen, D.V., Koster, G., Huijben, M., Bovet, N., et al. (2015). Extreme mobility enhancement of two-dimensional electron gases at oxide interfaces by charge-transfer-induced modulation doping. Nat. Mater. *14*, 801–806. https://doi.org/10.1038/nmat4303.
127. Chen, Y., Green, R.J., Sutarto, R., He, F., Linderoth, S., Sawatzky, G.A., and Pryds, N. (2017). Tuning the two-dimensional electron liquid at oxide interfaces by buffer-layer-engineered redox reactions. Nano Lett. *17*, 7062–7066. https://doi.org/10.1021/acs.nanolett.7b03744.
128. Liao, Z., Gauquelin, N., Green, R.J., Macke, S., Gonnissen, J., Thomas, S., Zhong, Z., Li, L., Si, L., Van Aert, S., et al. (2017). Thickness dependent properties in oxide heterostructures driven by structurally induced metal-oxygen hybridization vriations. Adv. Funct. Mater. *27*, 1606717. https://doi.org/10.1002/adfm.201606717.
129. Aghbolaghy, M., Soltan, J., and Sutarto, R. (2017). The role of surface carboxylates in catalytic ozonation of acetone on alumina-supported manganese oxide. Chem. Eng. Res. Des. *128*, 73–84. https://doi.org/10.1016/j.cherd.2017.10.002.
130. Zimmermann, P., Peredkov, S., Abdala, P.M., DeBeer, S., Tromp, M., Müller, C., and van Bokhoven, J.A. (2020). Modern X-ray spectroscopy: XAS and XES in the laboratory. Coord. Chem. Rev. *423*, 213466. https://doi.org/10.1016/j.ccr.2020.213466.
131. de Groot, F.M.F., Haverkort, M.W., Elnaggar, H., Juhin, A., Zhou, K.-J., and Glatzel, P. (2024). Resonant inelastic X-ray scattering. Nat. Rev. Methods Primers *4*, 45. https://doi.org/10.1038/s43586-024-00322-6.
132. Proux, O., Nassif, V., Prat, A., Ulrich, O., Lahera, E., Biquard, X., Menthonnex, J.-J., and Hazemann, J.-L. (2005). Feedback system of a liquid-nitrogen-cooled double-crystal monochromator: design and performances. J. Synchrotron Radiat. *13*, 59–68. https://doi.org/10.1107/s0909049505037441.
133. Weinhardt, L., Steininger, R., Kreikemeyer-Lorenzo, D., Mangold, S., Hauschild, D., Batchelor, D., Spangenberg, T., and Heske, C. (2021). X-SPEC: a 70 eV to 15 keV undulator beamline for X-ray and electron spectroscopies. J. Synchrotron Radiat. *28*, 609–617. https://doi.org/10.1107/s1600577520016318.
134. Szlachetko, J., Sá, J., Safonova, O.V., Smolentsev, G., Szlachetko, M., van Bokhoven, J.A., and Nachtegaal, M. (2013). In situ hard X-ray quick RIXS to probe dynamic changes in the electronic structure of functional materials. J. Electron. Spectrosc. Relat. Phenom. *188*, 161–165. https://doi.org/10.1016/j.elspec.2012.11.002.
135. Park, S.H., Yoon, J., Kim, C., Hwang, C., Kim, D.-H., Lee, S.-H., and Kwon, S. (2019). Scientific instruments for soft X-ray photon-in/photon-out spectroscopy on the PAL-XFEL. J. Synchrotron Radiat. *26*, 1031–1036. https://doi.org/10.1107/s1600577519004272.
136. Miyawaki, J., Suga, S., Fujiwara, H., Niwa, H., Kiuchi, H., and Harada, Y. (2017). A compact permanent-magnet system for measuring magnetic circular dichroism in resonant inelastic soft X-ray scattering. J. Synchrotron Radiat. *24*, 449–455. https://doi.org/10.1107/s1600577517000923.
137. Nowak, S.H., Armenta, R., Schwartz, C.P., Gallo, A., Abraham, B., Garcia-Esparza, A.T., Biasin, E., Prado, A., Maciel, A., Zhang, D., et al. (2020). A versatile Johansson-type tender x-ray emission spectrometer. Rev. Sci. Instrum. *91*, 033101. https://doi.org/10.1063/1.5121853.
138. Alonso-Mori, R., Kern, J., Sokaras, D., Weng, T.-C., Nordlund, D., Tran, R., Montanez, P., Delor, J., Yachandra, V.K., Yano, J., and Bergmann, U. (2012). A multi-crystal wavelength dispersive x-ray spectrometer. Rev. Sci. Instrum. *83*, 073114. https://doi.org/10.1063/1.4737630.